Imaging the Invisible: Constraining dark matter distributions in galaxy clusters using strong gravitational lensing

by

Virginia Leigh Corless

Submitted to the Department of Physics
in partial fulfillment of the requirements for the degree of

Bachelor of Science

at the

MASSACHUSETTS INSTITUTE OF TECHNOLOGY

[June 2005]
May 2005

Author .....
Department of Physics
May 13, 2005

Certified by .....
Saul A. Rappaport
Professor of Physics
Thesis Supervisor

Certified by .....
Scott M. Burles
Assistant Professor of Physics
Thesis Supervisor

Accepted by .....
Professor David E. Pritchard
Senior Thesis Coordinator, Department of Physics

Imaging the Invisible: Constraining dark matter distributions in galaxy clusters using strong gravitational lensing

by

Virginia Leigh Corless

Submitted to the Department of Physics
on May 13, 2005, in partial fulfillment of the
requirements for the degree of
Bachelor of Science

Abstract

In this thesis, I design and construct a Monte-Carlo gravitational lensing simulation that statistically studies the strong lensing of extended galactic sources by dark matter distributions in galaxy clusters, using recent work on cluster Abell 1689 as an empirical guide. By quantitatively comparing the quality of the lensed images created in the simulation to the giant lensed arcs observed by the Hubble Space Telescope around Abell 1689 and other similar clusters, and using an NFW analytic density profile to model the overall dark matter distribution, an upper limit is set on the scale of allowed deviations from a smooth NFW dark matter distribution. The maximum allowed mass-clumping is found to be on the order $\sim 10^8\ M_\odot$ over volumes of order $\sim$ 10kpc $\times$ 10kpc $\times$ 10kpc, indicative of a mostly smooth dark matter distribution with only relatively small deviations, much smaller than those of the distribution of conventional matter into galaxies.

Thesis Supervisor: Saul A. Rappaport
Title: Professor of Physics

Thesis Supervisor: Scott M. Burles
Title: Assistant Professor of Physics

Acknowledgments

I wish to thank Professor Paul Schechter and John Fregeau for imparting their knowledge of physics, cosmology, and numerical simulation to me throughout the course of my research. Thanks also to Jeffrey Blackburne, Justin Ashmall, Justin Kasper, and Michel Barrette for technical assistance and advice, and to Professor Lorne Nelson of the University of Sherbrooke for the use of his Beowulf cluster. Most especially I thank Professor Scott Burles for his advice and input in shaping the final form of this thesis, and Professor Saul Rappaport for his mentorship and guidance throughout the course of my research education at MIT. Finally, I dedicate this and my four years at MIT to my grandfather, Robert Mullen, who first taught me to gaze at the stars, and to my parents who gave me the tools to look even deeper.

Contents

List of Figures

List of Tables

Chapter 1

Galaxy Clusters and Dark Matter

1.1 A Dark History

It was in the 1920s, in the same days when the physics of the smallest scale of the Universe were being revolutionized by quantum mechanics, that astronomer Fritz Zwicky published a startling suggestion. He had measured the mass of the Coma galaxy cluster by observing the dynamical motion of its component galaxies, and obtained a value some ten times larger than that obtained by optical census of the cluster. His findings were met initially with great skepticism, due in part to his abrasive personality and in part to the radical implications of the result. His calculation suggested that some 90% of the galaxy cluster's mass was invisible to optical observation, a "dark matter" different from the stars previously thought to contain almost all of the matter in the universe [19].

Initial speculation focused on the gas and dust observed in the interstellar space within the Milky Way Galaxy as candidates to fill the intergalactic medium. Dust was quickly eliminated as a candidate because it absorbs heavily at optical wavelengths, making its presence directly observable, and no such obscuration was observed. Gas initially remained a possibility, but slowly, through decades of observation and the development of new technologies including X-ray astronomy, all of the emission lines indicative of the presence of molecular, neutral, or ionized hydrogen were found to be either altogether absent or present in quantities too small to account for the

observed dynamical mass of the galaxy clusters [14]. The only remaining conventional possibility were dark condensed objects, such as planets, brown dwarfs, or black holes, that might fill the intergalactic medium. However, it seemed unlikely that the intergalactic space would be filled with the large number of such objects necessary to account for the mass required by Zwicky's and others' dynamical calculations.

The mystery deepened when the cosmological theories of inflation and big-bang nucleosynthesis combined to impose requirements on the total amount of matter in the Universe. Inflationary theories demanded that the total density of the universe equal the critical density, $\rho/\rho_c = \Omega = 1$ [5], while calculations using the dynamically determined mass-to-light ratios of galaxy clusters found the total matter density of the Universe Ω_m to be only 0.3 [4]. Furthermore, the theories of big-bang nucleosynthesis combined with observations of the Cosmic Microwave Background and observations of the abundances of H, D, ^{3}He, and ^{4}He in the Universe to give a universal baryonic density Ω_b of only $\sim$ 0.04 [11], [16]. Thus, there was both missing density that was not matter at all, the so-called "dark energy", and a large amount of enigmatic missing matter composed of something other than the familiar baryonic particles, the building blocks of all conventional matter. Theory and observation thus converged to point to some new form of gravitating matter, comprising more than 90% of the matter density in the Universe, dark not for a mere lack of ignition or illumination, but rather because it was fundamentally different from the matter forming stars, planets, gas, dust (i.e., baryonic matter), and all other phenomena ever observed in the history of man. Suddenly the Universe that had only decades before been thought to be well understood was revealed to be saturated in a substance utterly foreign and unobserved.

1.2 A Continued Mystery

Decades later, this non-baryonic dark matter remains still very much a mystery because it is difficult to study. It interacts at best very weakly with conventional matter and photons, and is thus invisible to any form of electromagnetic observation, the pri-

mary observational method of virtually all of astronomy. Instead, it must be studied indirectly by observing its gravitational effects on conventional matter, and inferring from those effects an understanding of its motions and distribution in the Universe.

The gravitationally-governed dynamics of clusters are one such observable effect, and the dynamical calculations made first by Zwicky for the Coma cluster, and later by many others for other galaxy clusters, indicate that dark matter is distributed in a generally smooth distribution throughout each galaxy cluster. It is not primarily attached to the constituent galaxies of the cluster but rather fills the intergalactic medium. However, the details of its distribution are still unknown; fits of the overall distribution to theoretical mass profiles generated from dynamical N-body simulations of dark matter (see, e.g., NFW [10]) have provided a good understanding of the cluster-scale shape of the distribution, but the more detailed structure of the mass distribution on finer scales remains unclear. Measurements of galactic rotation curves [13] and of the x-ray emissions from hot gas in galaxy clusters provide some additional information, but even these combined with cluster dynamics cannot give good information regarding the smaller scale fluctuations in dark matter distributions, remnants of quantum oscillations during the inflationary epoch.

Luckily, there is another gravitational phenomena that is sensitive to dark matter distributions on smaller scales. It is gravitational lensing, the bending of light in a gravitational field described by Einstein's theory of general relativity. It can be understood in several ways, but the simplest and most useful for this investigation is to recognize that light always follows the path of extremal time as determined by a "far-away" observer. When mass curves spacetime around it, it changes the direction of the paths of extremal time, causing light to follow flight paths that are not "straight." Because the human eye and brain interpret all images as having been formed by light traveling on straight lines, the result of this bending is to create images of distant objects at locations at which they do not really exist. Gravitational lenses can even create multiple images of the same object, each magnified differently. The shape and location of those images is very sensitive to the nature of the mass distribution that bends the light to form them. Thus, by observing images lensed by

galaxy clusters, much can be learned about the dark matter distribution within those clusters.

1.3 Investigating the Smoothness of the Dark Matter Distribution

This thesis focuses particularly on one galaxy cluster, Abell 1689, recently cataloged in great detail by Broadhurst et al. [2]. It is a spectacular example of gravitational lensing, as the cluster is surrounded by images in the shapes of long arcs, distant galaxies that have been magnified and distorted by the cluster. The reason for the cluster's nickname as "The Great Zoom Lens in the Sky" is apparent in Figure 1-1, as it is observed by the Hubble Space Telescope (HST) to be encircled by the lensed images of dozens much more distant galaxies.

Broadhurst and his collaborators in their recent work carried out a detailed fit of the mass profile of Abell 1689 to a Navarro, Frenk, and White (NFW) mass distribution, one of several candidate analytic density profiles used to model the dark matter in galaxy clusters. Using this mass profile for the overall shape of the cluster in combination with smaller NFW halos around individual galaxies, it is possible to accurately model lensing by the galaxy cluster.

Characteristics of the smoothness of the overall NFW dark matter distribution may be studied theoretically by creating NFW mass distributions with varying magnitudes of density fluctuations from the smooth profile, varying the size of the mass elements used to create the overall distribution. By comparing the lensed images generated by such simulations with those observed surrounding Abell 1689 by the HST, interesting limits can be placed on the scale of the density fluctuations allowed in the dark matter distributions of galaxy clusters, and that is precisely what we set out to do in this thesis. We proceed by first laying out the basic physics of gravitational lensing and developing the necessary formalism to calculate image positions from a given source position and mass distribution in Section 2, followed by a discussion of

the known properties of the Abell 1689 galaxy cluster. In Section 3 we apply the general lensing formalism to an NFW profile constructed of Plummer spheres and detail the numerical lensing simulation. Finally, in Section 4 we present the results of the simulations, drawing conclusions about the smoothness of the dark matter distributions in lensing galaxy clusters and making suggestions for further work.

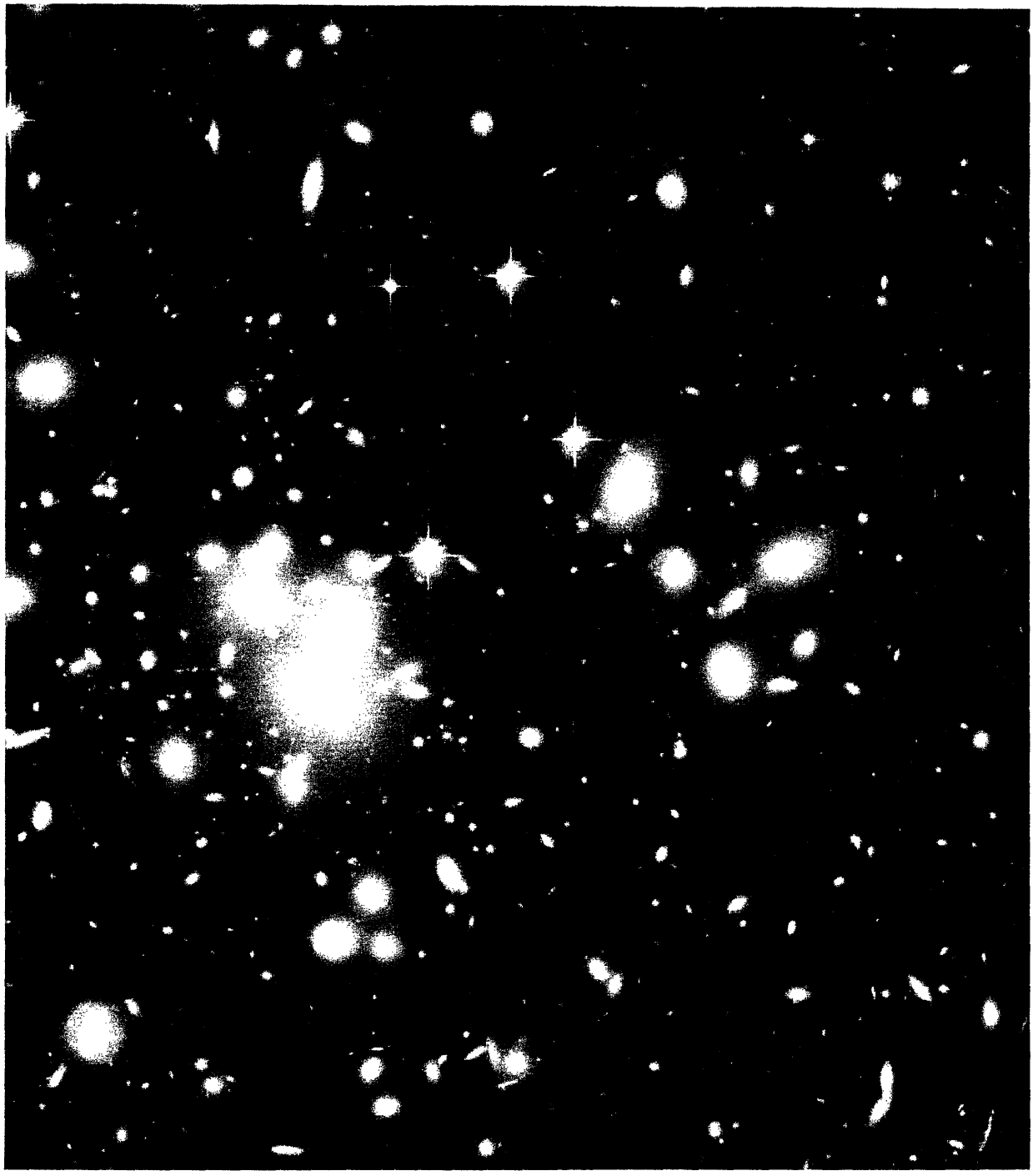

Figure 1-1: HST image of galaxy cluster Abell 1689. The field measures approximately $200'' \times 200''$. **Credit:** N. Benitez (JHU), T. Broadhurst (Hebrew Univ.), H. Ford (JHU), M. Clampin(STScI), G. Hartig (STScI), G. Illingworth(UCO/Lick), ACS Science Team, ESA, NASA.

Chapter 2

The Physics of Gravitational Lensing

The phenomenon of gravitational lensing was first predicted by Einstein in his theory of general relativity in the early years of the twentieth century. Lensing occurs when light, traveling through the curved spacetime around large masses as described by general relativity, is bent from its "straight" line path. The light following these curved paths is interpreted by observers on Earth as having followed a straight path (as all human observers unavoidably interpret what they see) and therefore appears to have come from a location other than its true source. The exact positions of such lensed images are determined by extremizing the time of flight from the source to the observer. Some lensing geometries allow multiple paths by which the time of travel is extremized, creating multiple images of the same source, some magnified, others de-magnified. Very large mass distribution create larger bending angles of the light and thus larger separations between images, making them easier to resolve. When the lensed source is located exactly on axis with a spherically symmetric lensing distribution, symmetry requires that, if the mass distribution is concentrated enough to cause lensing at all, there must be an entire ring of allowed paths, forming a single image of the source stretched into a complete "Einstein" ring centered on the source and coincident lens.

The fundamental physics of lensing was first confirmed on a small scale in 1919

when Sir Arthur Eddington and his research group observed the light from distant stars bend around the sun during a solar eclipse. As early as 1937 Fritz Zwicky [19] predicted that, as opposed to lensing by single stars, galaxies might be large enough to create multiple images of the same object at separations large enough to be individually resolved [3]. It took forty years before his prediction was confirmed, but in 1979 the first multiply imaged gravitationally lensed object was observed by Walsh et al. [17], a double image of quasar QSO 0957 +561 A+B lensed by a single galaxy. More discoveries followed quickly after. In 1980 Weymann et al. [18] observed what they believed to be, and was later confirmed as, the first quadruply lensed system, in which the quasar QSO 1115+080 was lensed into four resolved images by several intervening galaxies. The first Einstein ring, again of a quasar lensed by a single galaxy, was observed in 1988 by Hewitt et al. [6], and is pictured in Figure 2-1. Also shown in the panel of the same figure is another remarkable lensing situation in which both an Einstein ring and a quadruply lensed image are present. Large arcs, resolved images of whole galaxies rather than of point-like quasars, predicted to exist in 1937 by Zwicky, were first observed lensed by an entire galaxy cluster in 1986 by Lynds and Petrosian [9]. Many more such arcs were observed once the Hubble Space Telescope was launched in 1990. Figure 2-2 shows one such HST observation showing many lensed arcs surround galaxy cluster Abell 2218.

Both small and large mass distributions can cause lensing, but it is only large distributions that create resolvable multiple images of quasars or entire galaxies, the regime of strong lensing. Particularly, only galaxies or, more often, huge galaxy clusters comprised of dozens of constituent galaxies, are massive enough to create giant lensed arcs, the resolved images of very distant galaxies. These hugely massive galaxy cluster-lenses are also home to large distributions of dark matter, some attached to the constituent galaxies but most spread throughout the intergalactic medium [2]. It is the presence of this dark matter that brings us to develop the formalism of strong lensing, which we will use to build a lensing simulation to probe the details of the dark matter that invisibly magnifies, distorts, and multiplies images of even more distant galaxies.

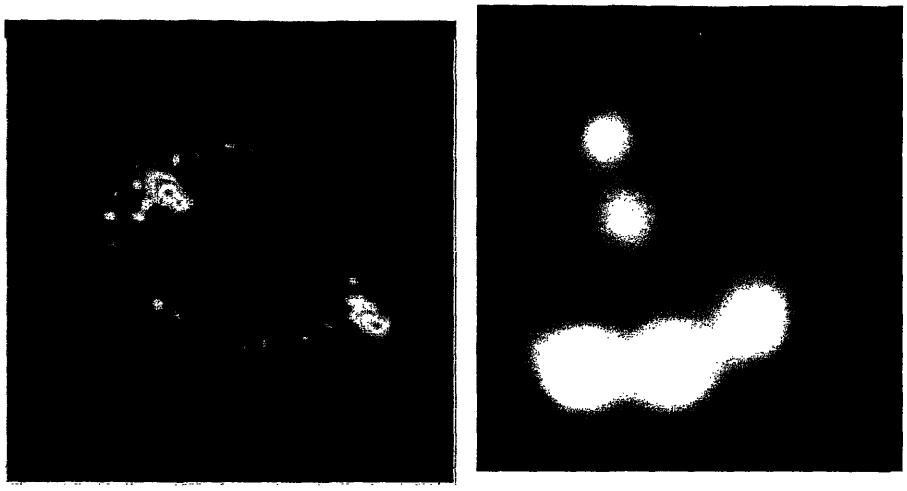

Figure 2-1: **Left:** The first observed Einstein ring [6]. **Right:** A remarkable image showing both an Einstein ring and a quadruple lensed image; the lensing galaxy can be seen in the center. Image courtesy of Paul Schechter. Discovered by [15].

2.1 General Lensing Formulation

Gravitational lensing is quantitatively described using the lens equation, which relates the positions of the lensed images to the original source position and the lensing mass distribution. To begin, we consider a distant source of light S, an observer on Earth $\mathcal{O}$, and an intervening mass distribution L, with distances defined as $\overline{\mathcal{O}L} = D_L$, $\overline{\mathcal{O}S} = D_S$, and $\overline{LS} = D_{LS}$, as shown in Figure 2-3. Light leaves S in all directions and travels on null geodesics calculable from each photon's initial position, direction of travel, and the mass distribution at L. There are an infinite number of such geodesics, but only a very few end at $\mathcal{O}$ on Earth where the observer can see them. It is only these geodesics that are of interest, for they will determine where the observer sees images of the source, lensed by the mass at L.

It is easiest to quantitatively approach the problem "backwards," considering all paths that lead from S to $\mathcal{O}$ and determining which are the null geodesics on which light actually travels. Null geodesics are by definition the paths of extremal travel time, and so the search for geodesics reduces to a problem in which the total travel time, affected by both the geometric path length and the relativistic slowdown of light due to the curvature of spacetime, is extremized. This extremization is easiest done

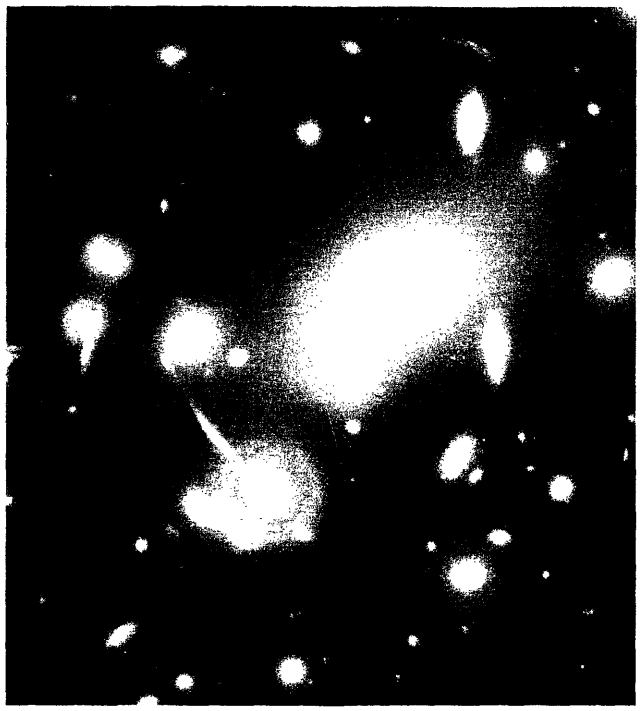

Figure 2-2: Abell 2218, a large galaxy cluster surrounded by lensed images of distant galaxies. **Credit:** Andrew Fruchter (STScI et al., WFPC2, HST, NASA.

by considering a general path consisting of two straight segments, first from the source at S to a bend point B, and then from B to the observer $\mathcal{O}$, writing down the analytic time delay as measured by the observer at $\mathcal{O}$ from both geometric and relativistic effects, and differentiating. This technique is valid only in the limit that the thickness of the lensing mass distribution is thin compared to the other distances, D_L and D_{LS}, involved in the problem (the "thin-lens" approximation), a good approximation when dealing with lensing systems in which the source is a very distant galaxy and the lens is a less distant galaxy cluster.

The relativistic delay can be calculated by dividing the lensing mass distribution into a large number of point masses and using the Schwarzschild metric associated with each of them to compute the apparent slowdown of light, and then summing over all of the component point masses. The slowdown of light due to one of these point masses can be characterized by an index of refraction $n \equiv c/v$ where v is the apparent

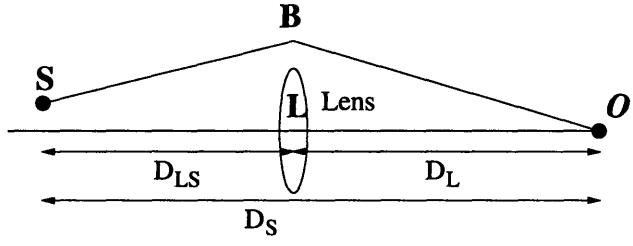

Figure 2-3: A simple lensing geometry.

velocity of the slowed light. This is solved for using the Schwarzschild metric

$$d\tau^2 = dt^2\left(1 - \frac{2M}{r}\right) - \frac{dr^2}{\left(1 - \frac{2M}{r}\right)} - r^2 d\phi^2 \tag{2.1}$$

for a null geodesic for which proper time $d\tau = 0$, giving

$$\frac{\left(\frac{dr}{dt}\right)^2}{\left(1 - \frac{2M}{r}\right)^2} + \frac{r^2\left(\frac{d\phi}{dt}\right)^2}{\left(1 - \frac{2M}{r}\right)} = 1 \quad . \tag{2.2}$$

For purely radial motion, for which $d\phi/dt = 0$ and $v = dr/dt$

$$n = \frac{1}{1 - \frac{2M}{r}} \simeq 1 + \frac{2M}{r} \tag{2.3}$$

where n is the effective index of refraction. Now, plugging in the constants G and c to obtain physical units, we find

$$n - 1 = \frac{2GM}{c^2 r} \quad . \tag{2.4}$$

Similar calculations yield a factor of 2 different n for purely azimuthal motion; however, because in the lensing geometry most of a photon's motion is in the radial direction, it is sufficient to use Equation 2.4 for all further calculations. Examination of Equation 2.4 quickly reveals that it is linearly proportional to the classical gravitational potential Ψ,

$$n - 1 = -\frac{2\Psi}{c^2} \tag{2.5}$$

where Ψ is a function of the photon's position in space as it travels from source to

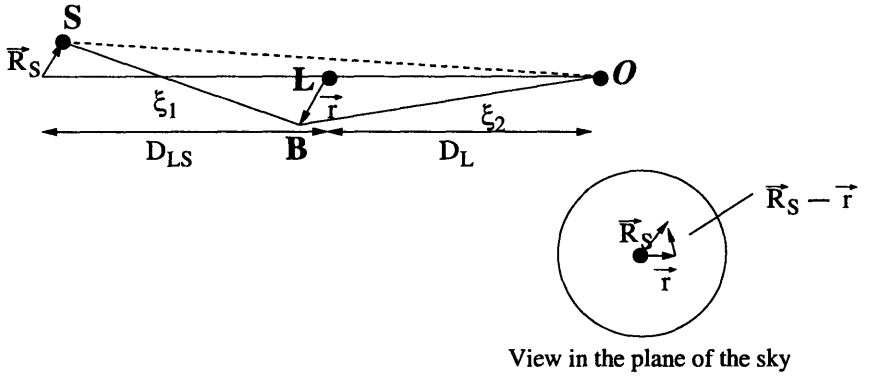

Figure 2-4: Calculating the Shapiro and geometric delays.

observer. To label this position it is convenient to define a vector $\vec{r}$, which gives the observed image location in the plane of the sky, and a scalar distance ξ along the path of travel, as illustrated in Figure 2-4. The relativistic time delay, also known as the Shapiro delay, for a path for which the distance from the bending point B to the lens L is equal to $\vec{r}$ is then given by

$$\tau_{shap}(\vec{r}) = \int \frac{n-1}{c} d\xi = -\frac{2}{c^3} \int \Psi(\vec{r},\xi) d\xi \equiv -\frac{2}{c^3} \Phi(\vec{r}) \quad . \tag{2.6}$$

where the integration is over the entire path from the source to the observer on Earth. $\Phi(\vec{r})$ is defined as the "lensing potential." We further make the approximation that the photon travels along straight line segments from S to B and then from B to O with an impact parameter $|\vec{r}|$.

Additionally, there is a geometric time delay that results from the extra path length traversed by a photon as it deviates from a single straight line path. The geometry of the delay is shown in Figure 2-4, and the extra path length can be written vectorially as

$$d = \sqrt{(\vec{R}_s - \vec{r})^2 + D_{LS}^2} + \sqrt{\vec{r}^2 + D_L^2} - \sqrt{(\vec{R}_s)^2 + D_S^2} \tag{2.7}$$

$$= D_{LS}\left[1 + \frac{(\vec{R}_s - \vec{r})^2}{D_{LS}^2}\right]^{1/2} + D_L\left(1 + \frac{\vec{r}^2}{D_L^2}\right)^{1/2} - D_S\left(1 + \frac{(\vec{R}_s)^2}{D_S^2}\right)^{1/2} \quad . \tag{2.8}$$

Taylor expanding and dividing by the velocity c gives the geometric time delay

$$\tau_{geom} \simeq \frac{(\vec{R}_s - \vec{r})^2}{2D_{LS}c} + \frac{\vec{r}^2}{2D_L c} + \frac{\vec{R}_s^{\,2}}{2D_S c} \quad . \tag{2.9}$$

The total time delay for a given path is then given by the sum of the Shapiro and geometric delays

$$\tau = \frac{(\vec{R}_s - \vec{r})^2}{2D_{LS}c} + \frac{\vec{r}^2}{2D_L c} + \frac{\vec{R}_s^{\,2}}{2D_S c} - \frac{2}{c^3}\Phi(\vec{r}) \quad . \tag{2.10}$$

We are now ready to find the extrema of the light travel times by differentiating with respect to $\vec{r}$, the image position in the source plane:

$$\vec{\nabla}_r \tau = 0 = \frac{\vec{r} - \vec{R}_s}{D_{LS}c} + \frac{\vec{r}}{D_L c} - \frac{2}{c^3}\vec{\nabla}_r \Phi(\vec{r}) \quad . \tag{2.11}$$

Collecting terms gives the source position $\vec{R}_s$ as a function of the image position and lensing potential

$$\vec{R}_s = \vec{r}\frac{D_S}{D_L} - \frac{2D_{LS}}{c^2}\vec{\nabla}_r \Phi(\vec{r}) \quad . \tag{2.12}$$

Finally dividing $\vec{R}_s$ by D_S and $\vec{r}$ by D_L, to turn all distances into angles as viewed on the sky from Earth, and converting the gradient to a derivative with respect to angle gives the lens equation in angular form

$$\vec{\theta}_s = \vec{\theta} - \frac{2D_{LS}}{D_S D_L c^2}\vec{\nabla}_\theta \Phi(\vec{\theta}) \quad . \tag{2.13}$$

The solutions to this equation define the image positions for a given source position and lensing potential. One can think of the entire plane of the sky as a Fermat surface of light travel times; images occur at local extrema on that surface. In the regime of strong lensing there are often multiple extrema, resulting in multiple images of the same source.

Two simple spherically symmetric cases are illustrative of the behavior of the

lensing equation. A point mass lens has gravitational potential

$$\Psi = -\frac{GM}{d} \tag{2.14}$$

so that its lensing potential is

$$\begin{aligned}
\Phi(r) &= -\int_0^{D_L} \frac{GMd\xi}{\sqrt{r^2-\xi^2}} - \int_0^{D_{LS}} \frac{GMd\xi}{\sqrt{r^2-\xi^2}} && (2.15)\\
&= -GM\left\{\ln\left[\xi+\sqrt{r^2+\xi^2}\right]_0^{D_L} + \ln\left[\xi+\sqrt{r^2+\xi^2}\right]_0^{D_{LS}}\right\} && (2.16)\\
&= -GM\left\{\ln\left[\frac{D_L+\sqrt{D_L^2+r^2}}{r}\right] + \ln\left[\frac{D_{LS}+\sqrt{D_{LS}^2+r^2}}{r}\right]\right\} && (2.17)\\
&\cong -GM\ln\left[\frac{4D_LD_{LS}}{r^2}\right] && (2.18)\\
&= GM\ln\left[\frac{r^2}{D_L^2}\right] - GM\ln\left[\frac{4D_{LS}}{D_L}\right] \quad . && (2.19)
\end{aligned}$$

The second term in the last line above is an unimportant constant, and the first can be easily expressed in terms of the angle $\theta = r/D_L$

$$\Phi(\theta) = GM\ln\theta^2 \tag{2.20}$$

giving the lens equation

$$\vec{\theta_s} = \vec{\theta} - \frac{4D_{LS}GM}{D_SD_Lc^2}\frac{\hat{\theta}}{\theta} \quad . \tag{2.21}$$

Finally, the spherical symmetry allows us to drop the vectors, giving simply

$$\theta_s = \theta - \frac{\theta_E^2}{\theta} \tag{2.22}$$

where θ_E is defined as the Einstein radius

$$\theta_E^2 \equiv \frac{4GMD_{LS}}{c^2D_SD_L} \quad . \tag{2.23}$$

In general, this simple lens equation has two solutions

$$\theta_1 = \frac{\theta_s}{2} + \frac{1}{2}\sqrt{\theta_s^2 + 4\theta_E^2} \tag{2.24}$$

$$\theta_2 = \frac{\theta_s}{2} - \frac{1}{2}\sqrt{\theta_s^2 + 4\theta_E^2} \quad . \tag{2.25}$$

When the source is located directly behind the lens, such that $\theta_s = 0$, the solution is then an Einstein ring with $\theta = \theta_E$. The Einstein radius thus gives a useful natural scale for lensing problems, because even when the lensing distribution is not a point mass or when the symmetry of the lensing situation is broken and the ring breaks into multiple arcs, the most interesting images and the largest magnifications occur at or near the Einstein ring radius.

The second instructive example is a generalization of the point mass to a "soft" mass distribution, called a Plummer sphere, with gravitational potential

$$\Psi(r) = -\frac{Gm}{(a^2 + r^2)^{1/2}} \quad . \tag{2.26}$$

These Plummer spheres will figure heavily in building the lensing model, and their lensing properties will be derived in detail in Section 3.1.3. The results are quoted here for purposes of illustration; for this potential the total delay is

$$\tau = \frac{D_S}{2cD_L D_{LS}}\left[(x - x_s)^2 + (y - y_s)^2\right] + \frac{2Gm}{c^3}\ln\left[\frac{4D_L D_{LS}}{a^2 + (x - x_s)^2 + (y - y_s)^2}\right] \tag{2.27}$$

and the 1D lensing equation in angular form is

$$\theta_s = \theta - \theta_E^2\left(\frac{\theta}{A^2 + \theta^2}\right) \tag{2.28}$$

where $A = a/D_L$. An on axis source ($\theta_s = 0$) will produce a ring image at $\theta = \sqrt{\theta_E^2 - A^2}$ if, and only if, $A < \theta_E$.

2.2 Galaxy Cluster Abell 1689

Abell 1689 is a rich galaxy cluster located at redshift $z = 0.18$ corresponding to a physical distance of about 600 Mpc. It contains a handful of large galaxies and hundreds of smaller ones, as well a great deal of dark matter. It is responsible for lensing dozens of galaxies behind it, with its huge mass stretching the images of some of them into long arcs.

In recent work by Broadhurst et al. [2] Abell 1689's large-scale mass distribution was fit to several analytic profiles and found to best fit an NFW profile, first proposed in 1996 by Navarro, Frenk, and White [10] in response to their own N-body simulations of dark matter distributions in galaxy clusters. Their profile accurately describes the overall mass distribution of dark matter phenomena ranging in scale from dwarf galaxy halos to rich galaxy clusters. As a tractable analytic model its major drawback is that it contains infinite mass when integrated over all space. However, this shortcoming can be easily overcome by setting an artificial cut-off radius, typically where the density of the cluster becomes equal to $18\pi^2$ times the cosmic average.

The NFW radial mass distribution, $\rho(r)$, is characterized by a scale radius r_s at which $r^2\rho(r)$ is maximum, and a scale density ρ_s defined as that at maximum density [8]:

$$\rho(r) = \frac{\rho_s}{\left(\frac{r}{r_s}\right)\left(1+\frac{r}{r_s}\right)^2} \quad . \tag{2.29}$$

The two scale quantities fit to the NFW profile for cluster Abell 1689 are $r_s = 310^{+140}_{-120}$ kpc$/h \approx 430$ kpc, observed as an angle on the sky of $\theta_s = 146'' \approx 150''$, and $\rho_s = 1.51 \times 10^6 M_\odot/\text{kpc}^3$. The cut-off radius is $8.2^{+2.1}_{-1.8} r_s$, and the total mass enclosed within that radius is $2.6 \times 10^{15} h M_\odot$, where the Hubble parameter is taken to be $H_0 = 72$ km/s/Mpc, $h = 0.72$ [2]. For purposes of comparison, a single galaxy of stars contains of order $10^{11} M_\odot$ for a Milky Way-type spiral, or $-10^{13} M_\odot$ for a giant elliptical, and has radius ~ 20 kpc.

The scale of the lensing geometry is set observationally by obtaining an approxi-

mate effective Einstein radius for the cluster, calculated empirically by averaging the radii of the most stretched lensed images observed around the cluster. Broadhurst finds that $\theta_E \simeq 50'' \approx 0.33\ \theta_s$ [2].

Equipped with a formulation of gravitational lensing and with an observationally shaped model for the dark matter distribution within Abell 1689, a paradigmatic lensing galaxy cluster, we are now ready to build a lensing simulation that should approximate the observations.

Chapter 3

Constructing the Lensing Model

3.1 Modeling Smoothness

Though the overall mass distribution of Abell 1689 is empirically determined, it is the goal of this thesis to better understand its smaller scale fluctuations. To do this, the lensing simulation must be designed to vary from clumpy to smooth mass distributions while always maintaining an overall profile consistent with the observed NFW profile. To allow this, discrete mass elements are distributed randomly according to an overall NFW density profile. By varying the size and number of the individual mass elements while always normalizing such that the total cluster mass remains the same, the smoothness of the mass distribution can be varied; a distribution consisting of 100 mass elements will be far less smooth than one consisting of 10^4, which will likewise be clumpier than one of 10^6 elements.

3.1.1 Monte Carlo Techniques

The discrete mass elements are randomly distributed in a profile consistent with an overall NFW distribution using a Monte-Carlo technique in which a uniform probability distribution is mapped into one matching a desired physical probability distribution. The standard technique as described in *Numerical Recipes* [12] requires integrating and inverting the desired probability distribution. This method is used

to create an isotropic angular distribution of mass elements in polar angle θ and azimuthal angle ϕ; however, it is not adequate for generating the proper radial distribution (Equation 2.29), which is not analytically invertible after integration. Thus, an alternate "dartboard" technique is employed.

It is beneficial to reduce the radial distance over which masses are distributed, because it allows the simulation of smoother profiles with fewer mass elements, leading to shorter calculation times. There is a theorem, whose proof is beyond the scope of this thesis, which states that only mass within the cylinder defined by the radius of the outermost lensed image contributes to the lensing, i.e., on the plane of the sky only matter enclosed within the radius of the outermost image is of any consequence to the lensing outcome. This theorem holds strictly for spherically symmetric mass distributions. For Abell 1689's Einstein radius of $\sim 0.33\ \theta_s$, it is thus very reasonable to distribute masses out to radii of only $2\theta_s$; while some mass located at radii greater than $2\theta_s$ would fall within the projected cylinder, it amounts to a very small fraction of the total mass in the cylinder ($\sim 0.05 M_{cylinder}$) because the density is small at large radii. This approximation will therefore not significantly affect lensing outcomes near $0.33\theta_s$, and greatly decreases the calculation times required for the simulation.

The probability of finding a mass element at a radius r is proportional to the density at that radius: high density implies more mass elements. To turn the NFW radial density function into a probability function ranging from $r = 0 \rightarrow r = 2r_s$, it is simply normalized to 1 when integrated over that interval:

$$\int \wp(r) = 1 = A \int_0^{2r_s} \frac{r^2 dr}{(r/r_s)(1 + r/r_s)^2} = A r_s^3 \int_0^2 \frac{x dx}{(1+x)^2} = A r_s^3 \left[\frac{1}{1+x} + \ln(1+x) \right]_0^2 \tag{3.1}$$

where $x = r/r_s$ and A is a normalization constant. Plugging in Abell 1689's scale radius $r_s \sim 430$ kpc, we have for the probability of finding a star between radius r and $r + dr$:

$$\wp(r) = \frac{0.00534(r/r_s)}{(1 + r/r_s)^2} \quad \text{kpc}^{-1} \quad . \tag{3.2}$$

To construct a distribution of mass elements consistent with this probability distribution, a dimensionless radius r/r_s and "probability" value are randomly chosen from

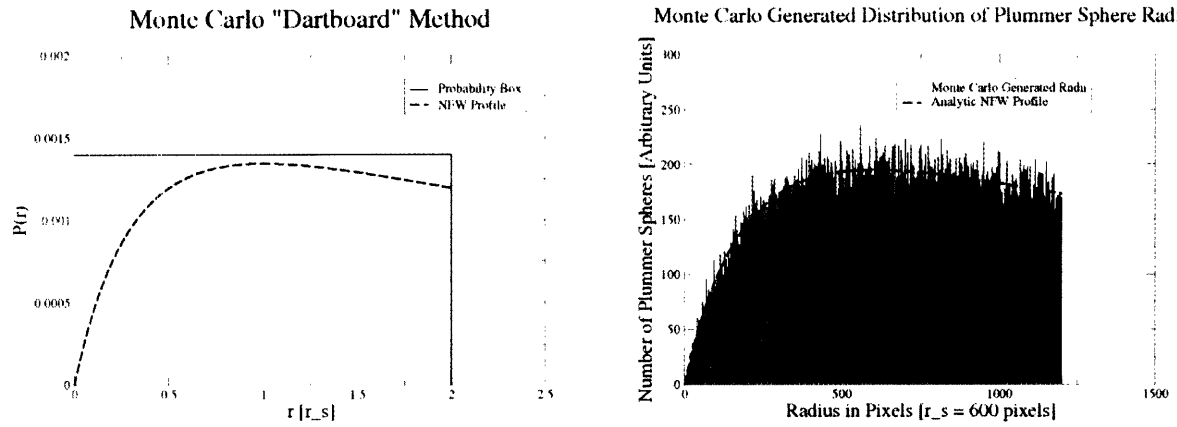

Figure 3-1: **Left:** The dartboard selection technique. Points are selected from within the probability box, and are retained only if they fall beneath the analytic NFW curve. **Right:** Analytic and Monte Carlo generated NFW integrated mass profiles.

uniform probability distributions ranging from $0 < r_s < 2$ and $0 < \wp(r) < 0.0014$, respectively, where 0.0014 is just larger than the maximum of Equation 3.2. The actual probability of finding a star at the selected radius is then calculated according to Equation 3.2 and compared to the randomly selected probability value. If the random probability is less than the calculated value, the radius is kept as the radius of a mass element in the galaxy cluster and assigned isotropically selected angular locations θ and ϕ; if not, it is discarded. In this system, radii at which mass is more likely to be found will be selected more often because the random probability will more frequently be less than the calculated actual probability. Figure 3-1 illustrates how this method of Monte-Carlo selection effectively fills in the area under the probability curve, leading to a random mass distribution consistent with the NFW density profile.

Once the three-dimensional coordinates of each mass element are randomly se-

lected, they are projected onto the lens plane according to the relations

$$x = r\cos\phi\sin\theta \tag{3.3}$$

$$y = r\sin\phi\sin\theta \tag{3.4}$$

$$\mathfrak{r} = \sqrt{x^2+y^2} \tag{3.5}$$

where the $\hat{z}$ axis lies along the line of sight and defines $\theta = 0$. If $\mathfrak{r} < 0.67r_s$ the mass element is added to the lensing distribution; if not, it is discarded. This process is repeated until N mass elements are distributed within a projected radius of $0.67r_s$, each with mass $m_n = M_{enc}/N_{2r_s}$, where N_{r_s} is the number of mass elements within a sphere of radius $2r_s$ and M_{enc} is the total mass enclosed within that sphere. Thus a cylinder of mass filled with N discrete mass elements is cut out of the full NFW mass distribution, projected as a circle on the sky that encloses all of the lensed arcs. This is the final step in the approximation begun by distributing mass elements out to radii of only $2r_s$, described above, which makes use of the fact that for spherically symmetric lenses only mass contained within the cylinder defined by the projected radius of the outermost lensed arc affects the lensing outcomes.

3.1.2 Defining the Mass Elements

In order to calculate the lensing effects of the NFW profile of discrete mass elements it is necessary to give the elements a definite density profile. For the sake of simplicity and flexibility, the Plummer profile is chosen as the shape of the individual mass elements [1]; it has a simple analytic form, contains finite mass when integrated over all space, has a built-in scale size, and is a simple spherically symmetric profile that may be as well-suited as any to characterize the mass "particles" forming the cluster's dark matter distribution. The density profile of a Plummer sphere is determined by a scale radius a that fixes the central density, and thus the overall "fluffiness" of the mass distribution

$$\rho(r) = \frac{2ma^2}{4\pi(a^2+r^2)^{5/2}} \quad ; \tag{3.6}$$

making a very small simulates point-like masses, while making it very large spreads the sphere's mass over a large volume in space. The 3D gravitational potential of such a Plummer sphere is

$$\Psi(r) = -\frac{Gm}{(a^2 + r^2)^{1/2}} \quad . \tag{3.7}$$

Now with a complete NFW distribution of well-defined Plummer spheres, all is ready to begin calculating the lensing effects of this simulated cluster on light traveling through its midst.

3.1.3 Lensing by Plummer Spheres

Equipped with the gravitational potential of the individual Plummer spheres, the lensing formalism from section 2.1 can be applied to determine the Shapiro delay due to a single sphere at position (x_n, y_n) in the lens plane. The 2D lensing potential for light passing by the Plummer sphere is

$$\begin{aligned}
\Phi(x,y) &= \int_0^{D_L} \Psi d\xi + \int_0^{D_{LS}} \Psi d\xi & (3.8)\\
&= \int_0^{D_L} -GM\frac{d\xi}{(a^2+b^2+\xi^2)^{1/2}} + \int_0^{D_{LS}} -GM\frac{d\xi}{(a^2+b^2+\xi^2)^{1/2}} & (3.9)\\
&= 2GM\left\{\ln\left[\frac{D_L + \sqrt{a^2+b^2+D_L}}{\sqrt{a^2+b^2}}\right] + \ln\left[\frac{D_{LS} + \sqrt{a^2+b^2+D_{LS}}}{\sqrt{a^2+b^2}}\right]\right\} & (3.10)
\end{aligned}$$

where b is the impact parameter of the ray passing the lens ($b^2 = (x - x_n)^2 + (y - y_n)^2$) where x and y give the position of the ray passing through the lens plane and x_n and y_n give the position of the nth Plummer sphere. Then taking $D_L \sim D_{LS} \gg \sqrt{a^2 + b^2}$

$$\Phi \approx -GM\left\{\ln\left[\frac{2D_L}{\sqrt{a^2+b^2}}\right] + \ln\left[\frac{2D_{LS}}{\sqrt{a^2+b^2}}\right]\right\} \tag{3.11}$$

and the time delay $\tau_{grav} = -\frac{2}{c^3}\Phi$ is

$$\tau_{grav} \approx \frac{2GM}{c^3}\ln\left[\frac{4D_L D_{LS}}{a^2+b^2}\right] \quad . \tag{3.12}$$

In addition to the relativistic (Shapiro) time delay, there is the additional geometric delay that results from the light taking a longer path through space as compared to a single straight line, as calculated in Equation 2.9. Expressed in (x, y) coordinates, where the source position is given by x_s and y_s, the geometric delay is

$$\tau_{geom} = \frac{1}{2c}\left[(x - x_s)^2 + (y - y_s)^2\right]\left(\frac{1}{D_{LS}} + \frac{1}{D_L}\right) \quad . \tag{3.13}$$

The total delay from both relativistic and geometric effects is then

$$\tau = \frac{D_S}{2cD_L D_{LS}}\left[(x - x_s)^2 + (y - y_s)^2\right] + \frac{2Gm_n}{c^3}\ln\left[\frac{4D_L d_{LS}}{a^2 + (x - x_n)^2 + (y - y_n)^2}\right] \quad . \tag{3.14}$$

To obtain the total lensing effect at an image plane location (x, y) the gravitational time delays from all of the N Plummer spheres are summed. The geometric part of the delay is counted only once because it has to do only with the geometry of the flight path of the light from source to observer, while each Plummer sphere in the cluster contributes to the Shapiro delay. The total delay from all of the mass in the NFW cluster is then

$$\tau = \frac{D_S}{2cD_L D_{LS}}\left[(x - x_s)^2 + (y - y_s)^2\right] + \sum_{n=1}^{N}\frac{2Gm_n}{c^3}\ln\left[\frac{4D_L D_{LS}}{a^2 + (x_n - x)^2 + (y_n - y)^2}\right] . \tag{3.15}$$

It is more convenient to express all of the position coordinates in terms of angles as seen on the sky. This is done by dividing all coordinate distances in the image plane by the distance from the observer to that plane D_L, giving

$$\tau = \frac{D_S D_L}{2cD_{LS}}\left[(X - X_s)^2 + (Y - Y_s)^2\right] + \sum_{n=1}^{N}\frac{2Gm_n}{c^3}\ln\left[\frac{4D_{LS}/D_L}{A^2 + (X_n - X)^2 + (Y_n - Y)^2}\right] . \tag{3.16}$$

Finally, minimizing the travel time τ, such that $\frac{\partial\tau}{\partial X} = \frac{\partial\tau}{\partial Y} = 0$, gives the complete equations determining the image positions for a source lensed by the entire NFW

distribution of Plummer spheres:

$$(X - X_s) - \frac{4GM_{enc}D_{LS}}{c^2 D_S D_L} \sum_{n=1}^{N} \frac{f_n(X - X_n)}{A^2 + (X_n - X)^2 + (Y_n - Y)^2} = 0 \tag{3.17}$$

$$(Y - Y_s) - \frac{4GM_{enc}D_{LS}}{c^2 D_S D_L} \sum_{n=1}^{N} \frac{f_n(Y - Y_n)}{A^2 + (X_n - X)^2 + (Y_n - Y)^2} = 0 \tag{3.18}$$

where $f_n \equiv m_n / M_{enc}$.

3.2 Simulation Strategy

3.2.1 Image Positions

Calculating image positions forward from knowledge of the positions of the source and lensing mass distribution is often quite difficult using Equations 3.17 and 3.18, because there is no way to solve analytically explicitly for X and Y. However, the equations are quite easy to solve backwards, starting with the location in the image plane (X, Y) and the positions of the lensing Plummer spheres, for the source position from which the light must have originated in order to arrive at that position:

$$X_s = X - \frac{4GM_{enc}D_{LS}}{c^2 D_S D_L} \sum_{n=1}^{N} \frac{f_n(X - X_n)}{A^2 + (X_n - X)^2 + (Y_n - Y)^2} \tag{3.19}$$

$$Y_s = Y - \frac{4GM_{enc}D_{LS}}{c^2 D_S D_L} \sum_{n=1}^{N} \frac{f_n(Y - Y_n)}{A^2 + (X_n - X)^2 + (Y_n - Y)^2} \quad . \tag{3.20}$$

We cycle through every pixel in the image plane, solve for the source position required by that image location, compare it to the actual position of our model source, and keep as image points only those pixels that project back to source locations within the model source, and thereby compute the appearance of the image.

3.2.2 Units

All of the physical quantities within the lensing simulation must be expressed in one set of units, easily convertible from the units of the code to real values. A natural unit of distance is the NFW scale radius r_s, and its angular counterpart $\theta_s = r_s/D_L$. By expressing all distances on the sky in terms of θ_s, the whole scale of the calculation can be set simply by setting θ_s equal to a certain number of pixels in the image plane of the simulation. As well, the prefactors of the NFW and Plummer lensing formulations must be scaled consistently.

Since the overall lensing geometry is defined by the NFW profile, we begin with that to define the natural units of the problem. For the NFW profile, the lensing potential, defined generally in section 2, is [8]

$$\Phi = 2\kappa_s r_s^2 \left[\ln^2\left(\frac{\ell}{2}\right) - \left(\tanh^{-1}\sqrt{1-\ell^2}\right)^2\right] \tag{3.21}$$

where ℓ is a dimensionless radius r/r_s and κ_s is a scaled surface density

$$\kappa_s = \frac{\rho_s r_s 4\pi G D_L D_{LS}}{c^2 D_S} \quad . \tag{3.22}$$

Plugging this into the lensing equation, Equation 2.12, gives

$$r_{source} = r - \frac{8\pi G\rho_s r_s^2 D_L D_{LS}}{c^2 D_S}\frac{d}{d\ell}\left[\ln^2\left(\frac{\ell}{2}\right) - \left(\tanh^{-1}\sqrt{1-\ell^2}\right)^2\right] \tag{3.23}$$

where $\frac{d}{d\ell} = r_s\frac{d}{dr}$. Completing the differentiation and dividing through the whole equation by r_s gives the lensing equation in dimensionless units

$$\ell_{source} = \ell - \frac{8\pi G\rho_s r_s D_L D_{LS}}{c^2 D_S}\left[\frac{2\ln\left(\frac{\ell}{2}\right)}{\ell} + \frac{2\tanh^{-1}\sqrt{1-\ell^2}}{l\sqrt{1-\ell^2}}\right]. \tag{3.24}$$

Converting to an angular scale such that all distances are in units of θ_s, such that $\theta = r/D_L = \frac{r}{r_s}\frac{r_s}{D_L} = \ell\theta_s$, the variable ℓ should now to be interpreted as $\theta/\theta_s \equiv \Theta$. It

is convenient to group the prefactors in Equation 3.24 into a single constant

$$T_s = \sqrt{\frac{c^2 D_S}{8\pi G \rho_s r_s D_L D_{LS}}}. \tag{3.25}$$

The NFW lensing equation in units of θ_s then becomes simply

$$\Theta_{source} = \Theta - \frac{1}{T_s^2}\left[\frac{2\ln\left(\frac{\Theta}{2}\right)}{\Theta} + \frac{2\tanh^{-1}\sqrt{1-\Theta^2}}{\Theta\sqrt{1-\Theta^2}}\right] \tag{3.26}$$

which can also be expressed more conveniently in terms of logarithmic functions as

$$\Theta_{source} = \Theta - \frac{1}{T_s^2}\left[\frac{2\ln\left(\frac{\Theta}{2}\right)}{\Theta} + \frac{\ln\left[\frac{1+\sqrt{1-\Theta^2}}{1-\sqrt{1-\Theta^2}}\right]}{\Theta\sqrt{1-\Theta^2}}\right] \tag{3.27}$$

To allow for consistent calculations throughout the code, it is then necessary to express the equations for lensing by Plummer spheres, Equations 3.17 and 3.18, in terms of the natural NFW scale factor T_s and angular scale θ_s. Because both equations are given in units of angle on the sky, we first divide all angles by $\theta_s = r_s/D_L$ to put them in dimensionless units of θ_s. The prefactor in front of the summation term can then be rewritten

$$\frac{4GM_{enc}D_{LS}}{c^2 D_S D_L} = \frac{16\pi G I \rho_s r_s D_{LS} D_L}{c^2 D_S} = \frac{2I}{T_s^2} \tag{3.28}$$

where I is the integral

$$\int_0^k \frac{x\,dx}{1+x} = \left[\frac{1}{1+x} + \ln(1+x)\right]_0^k \quad , \tag{3.29}$$

and where k is the number of scale radii to which the Plummer spheres are distributed in the simulation. For the lensing simulation in which $k = 2$, $I = 0.4319$. The Plummer lensing equations can then be written entirely in terms of T_s, which can be calculated from the red-shift determined distances of the Abell 1689 cluster ($z = 0.18$), its lensed sources ($1.0 < z < 5.0$), and the scale angular distance $\theta_s = 150''$. The latter quantity is set to a specified number of pixels within the lensing simulation to fix the pixelated scale of the cluster, the source, and the lensed images. The Plummer

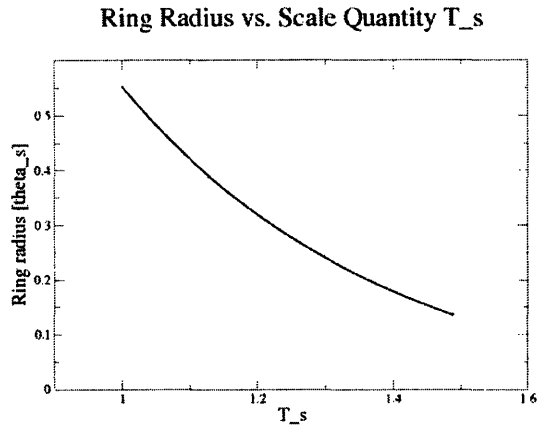

Figure 3-2: The radius of the Einstein ring formed by a point source located exactly on axis behind an NFW lens as a function of the NFW scale quantity T_s.

lensing equations in units of θ_s are:

$$\Theta_{x,s} = \Theta_x - \frac{2I}{T_s^2} \sum_n \frac{f_n(\Theta_x - \Theta_{x,n})}{\Theta_A^2 + (\Theta_{x,n} - \Theta_x)^2 + (\Theta_{y,n} - \Theta_y)^2} \tag{3.30}$$

$$\Theta_{y,s} = \Theta_y - \frac{2I}{T_s^2} \sum_n \frac{f_n(\Theta_y - \Theta_{y,n})}{\Theta_A^2 + (\Theta_{x,n} - \Theta_x)^2 + (\Theta_{y,n} - \Theta_y)^2}. \tag{3.31}$$

The Einstein ring radius for a source located perfectly on axis for an NFW lensing profile is given as a function of T_s by setting $\Theta_s = 0$ in the symmetric NFW lens equation, Equation 3.27. This equation can be numerically solved for Θ for a given T_s, and the results are shown in Figure 3-2. The empirically determined average Einstein radius of Abell 1689 is $50'' \simeq 0.33\ \theta_s$, which from the plot is seen to correspond to a T_s value of approximately 1.2; this value is adopted in the lensing simulation. That T_s is a dimensionless quantity of order unity can be seen from the following expression:

$$T_s \cong 1.2 \left(\frac{\rho_s}{1.5 \times 10^6 M_\odot/\mathrm{kpc}^3}\right)^{-1/2} \left(\frac{r_s}{430\ \mathrm{kpc}}\right)^{-1/2} \left(\frac{D_L}{0.6\ \mathrm{Gpc}}\right)^{-1/2} \left(\frac{D_S}{1.5\mathrm{Gpc}}\right)^{1/2} \left(\frac{D_{LS}}{1.3\ \mathrm{Gpc}}\right)^{-1/2} \tag{3.32}$$

Distances to the lens and source are calculated as comoving distances D_A, given

Table 3.1: The NFW scale radius and Einstein radius of the simulated lensing cluster in physical, angular, and pixel units.

	Physical Units	Angular Units	Pixels
r_s	430 kpc	$\sim 150''$	600 pixels
θ_E	145 kpc	$50''$	200 pixels

by

$$D_A = \frac{D_H}{1+z} \int_0^z \frac{dz'}{\sqrt{\Omega_M (1+z)^3 + \Omega_\Lambda}} \quad , \tag{3.33}$$

where z is the cosmological redshift, Ω_k is taken to be zero, and $D_H \equiv c/H_0 = 3000$ Mpc/h [7]. Taking $\Omega_M = 0.3$ and $\Omega_\Lambda = 0.7$, D_L for the lens at redshift $z = 0.18$ is 609 Mpc. For a source at $z = 1$, $D_S = 1607$ Mpc and $D_{LS} = 1248$ Mpc; for a more distant source with $z = 2$, $D_S = 1680$ Mpc and $D_{LS} = 1440$ Mpc. Importantly however, the lensing results of the simulation do not depend on the choice of distance measure. Rather, by choosing T_s, the quantity in the lensing equations that depends directly on the distances of the lens and source from the observer and each other, using Figure 3-2 such that the lensed arcs occur near the Einstein radius measured for Abell 1689, we guarantee that the numerical value for T_s is correct.

Finally, θ_s is set to 600 pixels, such that in a 500×500 pixel grid only objects within somewhat less than one scale radius of the NFW potential will be observed, and the lensed arcs appear at radii near 200 pixels. The key scale quantities of the simulation are given in physical, angular, and pixel units in Table 3.1.

3.2.3 Source Position and Size

The sources used in the calculation are simple spheres, circles when projected onto the plane of the sky, roughened at the edges by the discrete nature of pixels in the source plane. Three source sizes are used, with radii of 1, 5, and 10 pixels, and their surface brightness is taken to be constant. They are located slightly off the center of the cluster; were they centered, they would result in a complete Einstein ring. Some of the images observed in Abell 1689 are extremely long arcs, remnants of an

Einstein ring, but broken by the asymmetry of a source located somewhat off axis of the cluster; thus, the sources in the simulation are located similarly.

3.2.4 Assessing the Lensed Images

We are interested not only in qualitatively observing the image patterns formed by a circular source, but also in quantitatively describing the "quality" of that image. The natural scale for "quality" is that set by the images formed by a perfectly smooth lensing mass distribution. These highest quality images are smooth and uniform arcs, free of ragged edges or uneven surface brightness. As observed by the Hubble Space Telescope, the lensed images of Abell 1689 are very close to this standard of high quality: very smooth, without ragged edges or irregularities to within the $\sim 0.05''$ angular resolution of the optics. We thus seek to identify a level of quality in our simulated images that matches the observed level in the HST images, allowing us to link the simulated granularity in our mass distributions to the actual granularity in the overall NFW mass distribution responsible for the lensing in Abell 1689.

Quantifying the quality of the large lensed arcs generated by the code is a difficult proposition. With thousands of pixels in each image and irregularly shaped arcs, no simple metric presents itself. It is therefore desirable to find a simpler frame in which to analyze the images. One natural such frame is the source plane, in which the large imaged arcs are compressed back into the compact circular source from which they were lensed. If the images are of the highest quality, when projected back through an ideal NFW profile they should fall uniformly within the original source. By measuring the deviation of the back projected source from the original, a simple measure of the quality of the image can be constructed.

Images are projected back into the source plane by plugging the location of each image pixel in units of θ_s into the lensing equation for a smooth NFW mass profile as given in Equation 3.26, in units of θ_s and separated into two equations for Θ_x and

Θ_y.

$$\Theta_{x,s} = \Theta_x \left\{ 1 - \frac{2}{T_s^2(\Theta_x^2 + \Theta_y^2)} \left[\ln\left(\frac{\sqrt{\Theta_x^2 + \Theta_y^2}}{2} \right) + \frac{\tanh^{-1}\sqrt{1 - \Theta_x^2 - \Theta_y^2}}{\sqrt{1 - \Theta_x^2 - \Theta_y^2}} \right] \right\} \tag{3.34}$$

$$\Theta_{y,s} = \Theta_y \left\{ 1 - \frac{2}{T_s^2(\Theta_x^2 + \Theta_y^2)} \left[\ln\left(\frac{\sqrt{\Theta_x^2 + \Theta_y^2}}{2} \right) + \frac{\tanh^{-1}\sqrt{1 - \Theta_x^2 - \Theta_y^2}}{\sqrt{1 - \Theta_x^2 - \Theta_y^2}} \right] \right\} \tag{3.35}$$

To best quantify the deviation of the back projected source from the original, it is necessary to construct measures of both the overall size of the projected source and its asymmetry. A simple measure of the size of the source is the root-mean-square radius $\mathfrak{r}_{RMS}$ of all of the points in the projected source

$$\mathfrak{r}_{RMS} = \sqrt{\frac{\sum_{i=1}^{N} \mathfrak{r}_i^2}{N}} \tag{3.36}$$

where $\mathfrak{r}_i$ is measured from the center of the original lensed source. For a uniform circle of radius R, $\mathfrak{r}_{RMS} = R/\sqrt{2}$, giving a source of radius 10 pixels = 0.02 θ_s a minimum $\mathfrak{r}_{RMS}$ of 7.1 pixels. To quantify the asymmetry of the source the quadrupole moment is a logical choice, defined for a finite distribution in a two-dimensional plane as

$$Q_{ij} \equiv \sum_{k}^{N} (2\mathfrak{r}_{ik}\mathfrak{r}_{jk} - \mathfrak{r}_k^2 \delta_{ij}) \tag{3.37}$$

where i and j equal 1 or 2. The three independent components are

$$Q_1 = \sum_{k}^{N} (2x_k^2 - \mathfrak{r}_k^2) = \sum_{k}^{N} (x_k^2 - y_k^2) \tag{3.38}$$

$$Q_2 = \sum_{k}^{N} (2x_k y_k) \tag{3.39}$$

$$Q_3 = \sum_{k}^{N} (2y_k^2 - \mathfrak{r}_k^2) = \sum_{k}^{N} (y_k^2 - x_k^2) \tag{3.40}$$

Because Q_1 and Q_3 are antisymmetric it is only necessary to calculate Q_1 and Q_2 to obtain all relevant information about the projected source. Furthermore, because

various lensed images will have different numbers of "lit" pixels in them, and consequentially different numbers of pixels projected back into the source plane, the quadrupole moments are normalized by $1/N$ to allow useful comparison among images of different sizes.

3.2.5 Quantifying the Mass Distributions

Once we have identified which lensed images created by the code are consistent with the long arcs observed in Abell 1689, it remains to understand the nature of the mass distributions that created those images. While all of the mass distributions simulated follow an overall NFW profile, they vary significantly in their smoothness, and it is precisely this smoothness that we seek to quantify and set limits on in nature.

We define the shape of a smooth mass distribution as that of the analytic NFW density profile

$$\wp(r)dr = \frac{r^2}{\left(\frac{r}{r_s}\right)\left(1+\frac{r}{r_s}\right)^{1/2}}dr \quad , \tag{3.41}$$

first introduced in Section 2.2. Integrating along the direction into the plane of the sky gives the 2D surface density

$$\wp(\mathfrak{r}) = A\left[\frac{1}{\mathfrak{r}^2-1} - \frac{\sec^{-1}(\mathfrak{r})}{(\mathfrak{r}^2-1)^{3/2}}\right] \quad . \tag{3.42}$$

Deviations from this analytic surface density profile will be quantified to give a measure of the percentage deviation from smoothness of all of the mass distributions constructed in the lensing simulation.

The deviations are measured by comparing the mass in each pixel in the annulus between radii of 150-250 pixels $[(0.25-0.42)r_s]$ to that predicted to be present by Equation 3.42. The deviation is not calculated over the entire range of the simulated density profile because we are, in fact, interested mostly in the density fluctuations near the image positions. Limiting the range of the deviation measurement in this way is also desirable because it avoids measuring the large deviations that occur at very small radii due to the very large density near $r = 0$ and finite pixel size that

limits the quantity of mass elements at those small radii in the simulation. The analytic density profile is normalized to the mass scale of the lensing simulations by performing a least-squares fit of the mass distributions of cluster models with $\sim 2 \times 10^7$ Plummer spheres distributed within $2r_s$ ($N = 10^7$) to the analytic form multiplied by a normalization constant A. The average value of the normalization constants determined in this manner for several large-N runs is taken as the universal normalization, and it multiplied by the analytic form is defined as the standard of smoothness.

Deviations from this standard are quantified by calculating the percentage root-mean-square deviation of the simulated mass profile from the smooth distribution in each pixel over the area of the annulus between radii of 150-250 pixels

$$\delta M_{RMS} = \sqrt{\frac{\left[\left(\frac{\text{Simulated Mass Profile}}{\text{Standard Mass Profile}} - 1.0\right) \times 100\right]^2}{N}} \quad . \tag{3.43}$$

This measure thus gives the percentage root-mean-square deviation of the mass distribution of the simulated cluster over the entire surface area of the lensed arcs, measured on the spatial scale of single pixels. Each pixel in the simulation corresponds to a physical area of approximately 0.22 kpc $\times$ 0.22 kpc, and the area of the entire annulus is ~ 60 Mpc^2.

Chapter 4

Results of the Lensing Simulation

4.1 Four Lensing Models

A series of lensing simulations were run varying the size of the lensed source, the number and size of the lensing Plummer spheres, and the random seed used to distribute the Plummer spheres within the NFW profile, in order to generate four separate lensing scenarios in which the lensed image quality can be compared with the smoothness of the lensing mass distribution. The four lensing models are listed in Table 4.1; in them the radius of the source R_{source} is set to 10, 5, or 1 pixels in the source plane, the source is located either 2.50″ or 0.60″ from the center of the lens, and the size of the lensing Plummer spheres is varied between two values, controlled by the scale parameter a as it appears in Equation 3.6.

The relative size of a is best understood in relation to the Einstein radius θ_E of

Table 4.1: Four lensing models

Model	Source radius [pixels]	Source radius [″]	Source position [″]	Plummer radius a $[\theta_s a_0]$
1	10	2.50″	2.50″	0.2
2	5	1.25″	2.50″	0.2
3	1	0.25″	0.60″	0.2
4	10	2.50″	2.50″	0.02

an individual Plummer sphere in a lensing geometry, defined in Equation 2.23 as

$$\theta_E^2 \equiv \frac{4GMD_{LS}}{c^2 D_S D_L} \quad . \tag{4.1}$$

When $a > \theta_E$, no lensing occurs. Thus, when the scale radii of the individual Plummer spheres within the overall NFW distribution are larger than their individual Einstein radii, no micro-lensing by individual mass elements can occur; only strong lensing by the entire mass distribution is present. The physical scale of θ_E can be usefully understood in terms of the angular resolution of the observing telescope, equal to $0.05''$ for the HST. If $\theta_E <$ angular resolution of HST ($\sim 0.05''$) then images lensed by an individual Plummer sphere will not be resolved. For the first three lensing scenarios

$$a = 0.1\frac{(2\theta_s)}{N_{2r_s}^{1/3}} = 0.2\theta_s N_{2r_s}^{-1/3} \equiv 0.2\theta_s a_0 \quad , \tag{4.2}$$

where N_{2r_s} is the number of Plummer spheres contained within radius $2r_s$. At this scale radius the Plummer spheres approximately fill most of the volume within $2r_s$, and a is greather than θ_E, making micro-lensing impossible. In the fourth model a is reduced by a factor of 10 so that

$$a = 0.02\theta_s a_0 < \theta_E \quad , \tag{4.3}$$

such that the Plummer spheres act more like point-like masses, each independently capable of micro-lensing background sources into unresolved images in addition to the strong lensing carried out by the entire cluster.

An additional radius tht affects the ability of individual Plummer spheres to micro-lens is that of the source. If the angular size of the source is larger than the Einstein radius of the Plummer sphere, only a fraction of the surface brightness from the source can be magnified by the lensing sphere, because only those light rays that pass the lens at impact parameters less than the Einstein radius will be significantly magnifed.

Because lensing is only dependent on the lensing mass contained within the pro-

Table 4.2: The Plummer scale radius a, the Einstein radius θ_E, and the mass m_n of an individual Plummer sphere for each value of N.

N	θ_E [″]	$a = 0.2\theta_s a_0$ [″]	$a = 0.02\theta_s a_0$ [″]	m_n [$M_\odot$]
10^2	6.23″	4.76″	0.48″	3.4×10^{12}
3×10^2	3.60″	3.30″	0.33″	1.2×10^{12}
10^3	1.97″	2.21″	0.22″	3.4×10^{11}
3×10^3	1.14″	1.53″	0.15″	1.2×10^{11}
10^4	0.62″	1.03″	0.10″	3.5×10^{10}
3×10^4	0.36″	0.71″	0.07″	1.2×10^{10}
10^5	0.20″	0.48″	0.05″	3.5×10^{9}
3×10^5	0.11″	0.33″	0.03″	1.2×10^{9}
10^6	0.06″	0.22″	0.02″	3.5×10^{8}
3×10^6	0.04″	0.15″	0.02″	1.2×10^{8}
10^7	0.02″	0.10″	0.01″	3.5×10^{7}

jected angular radius of the lensed images, 0.33 θ_s, smoother profiles at every N are obtained by carrying out calculations only for Plummer spheres whose projected angular radii are less than 0.67 θ_s, as discussed in Section 3.1.1. For each of the four models described above, lensing is calculated for distributions of $N = 10^2$, 3×10^2, 10^3, 3×10^3, 10^4, 3×10^4, 10^5, 3×10^5, 10^6, 3×10^6, and 10^7 Plummer spheres within 0.67 θ_s. The mass of each Plummer sphere is given by $m_n = \frac{0.3253 M_{cluster}}{N_{2r_s}}$, where $N_{2r_s} \approx 2.5N$; the values of m_n are given in Table 4.2. The factor of 0.3253 arises from calculating the fraction of total cluster mass contained within radius $2r_s$. For each combination of source size, position, and Plummer sphere size and number, six statistical trials–of different random distributions–of Plummer spheres were run.

Each such lensing simulation generated output files giving the surface mass density of the lensing mass distribution, the original source position, the lensed images, and the back-projected source of those images. That output is shown in Figure 4-1 for a source 10 pixels in radius, projected through 10^5 Plummer spheres.

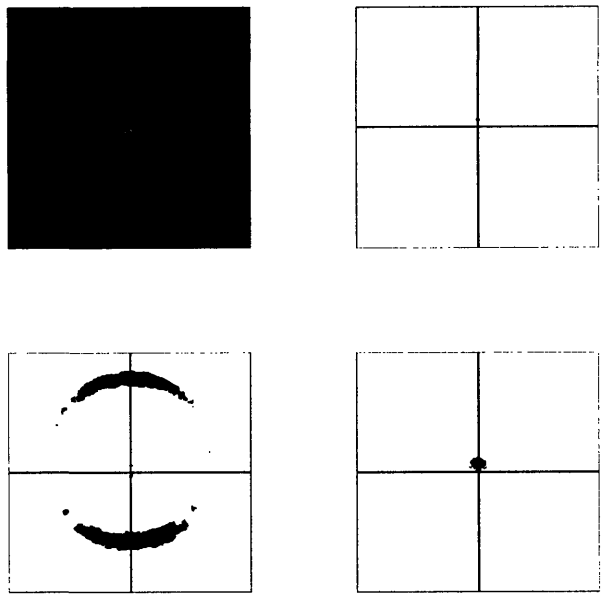

Figure 4-1: Lensing simulation with source radius $R_{source} = 10$ pixels, $a = 0.2\theta_s a_0$, and $N = 10^5$. **UL:** Projected mass distribution. **UR:** Original source. **LL:** Lensed images. **LR:** Projected source of the lensed images, projected back through a smooth NFW potential.

4.2 Quantifying Deviations in the Simulated Mass Distributions

The four sets of parameters for which the full range of N values were run are, as given in Table 4.1: $R_{source} = 10$ pixels, $a = 0.2\theta_s a_0$; $R_{source} = 5$ pixels, $a = 0.2\theta_s a_0$; $R_{source} = 1$ pixel, $a = 0.2\theta_s a_0$; $R_{source} = 10$ pixels, $a = 0.02\theta_s a_0$. These represent a large, mid-sized, and small source lensed by a lumpy, but nearly continuous, fluid medium, and a large source lensed by a distribution of point-like masses. For each, the mass distributions are quantified as described in section 3.2.5, using the $N = 10^7$ mass distributions to normalize the analytic mass distribution and thereby determine the "smooth" mass profile. The percentage RMS deviation from this smooth profile for all of the smaller-N runs is then computed. A plot of a fitted NFW profile is shown in Figure 4-2 for $R_{source} = 10$ pixels, $a = 0.2\theta_s a_0$, plotted with the mass profile along a single radial line in the annulus between radii of 150-250 pixels for distributions of $N = 10^3$, 10^4, 10^5, and 10^6 Plummer spheres.

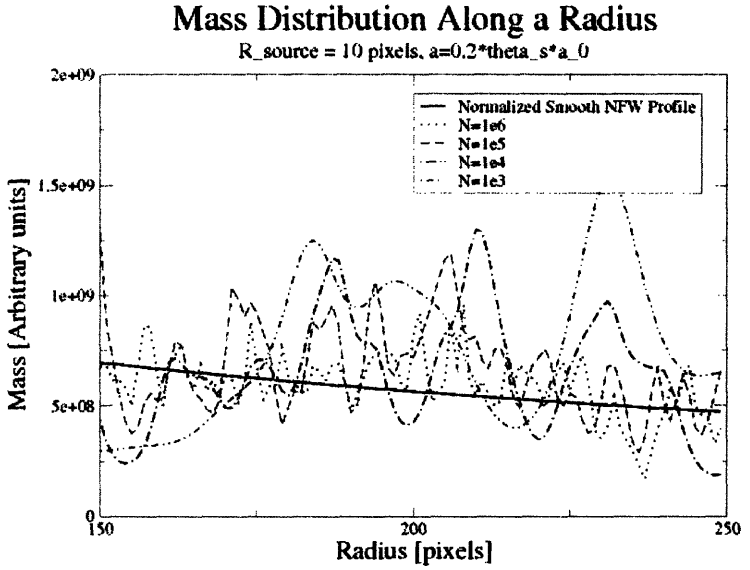

Figure 4-2: **Left:** A normalized smooth NFW mass profile, plotted with the density profiles along a single radial line for distributions of $N = 10^3$, 10^4, 10^5, and 10^6 Plummer spheres with $R_{source} = 10$ pixels and $a = 0.2\theta_s a_0$.

The mass profiles for the mass distributions from which those radial mass profiles are drawn have root-mean-square deviations $\delta M_{RMS} = 73\%$, 53%, 37%, and 25% respectively. In Figure 4-3 the surface densities of those profiles, the lensed images created by them, and the back projection of those images into the source plane through a smooth NFW profile are plotted. In them it is apparent that the images become significantly cleaner and more uniform as N, and the smoothness of the mass distribution, increases.

4.3 Quality of the Simulated Images

The key step to extracting physically meaningfully information from these simulated data is to compare the simulated lensed images to those seen in the actual HST observations of Abell 1689. Two of the many lensed giant arcs from the Hubble Deep Advanced Camera image are shown in Figure 4-4. They are seen to be quite smooth, uniform in their surface brightness, and not ragged at their edges. This description

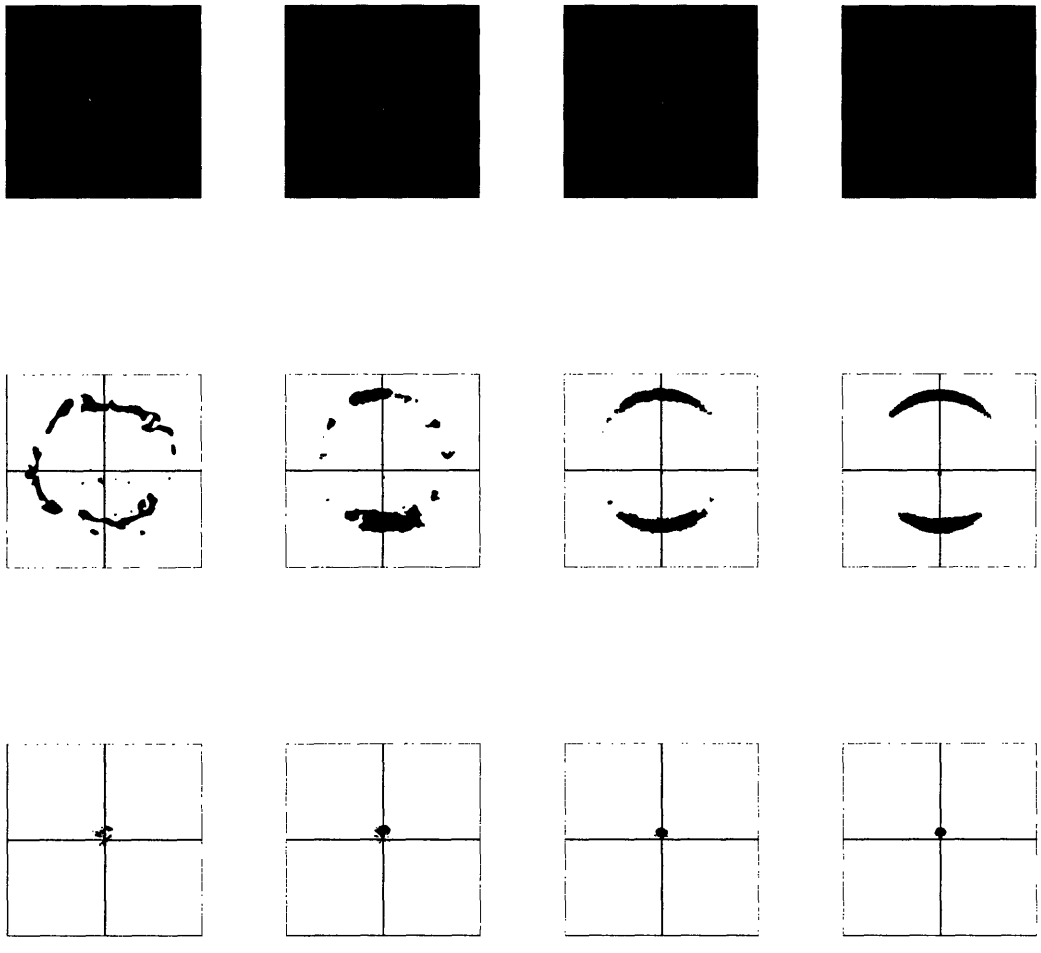

Figure 4-3: The projected density profiles, lensed images, and back-projected sources for distributions of $N = 10^3$, 10^4, 10^4, and 10^6 Plummer spheres lensing a source with $R_{source} = 10$ pixels, $a = 0.2\theta_s a_0$.

is true of most of the lensed images in the HST photographs. We seek to match that smoothness in our simulated images. The pixels in the HST images are approximately

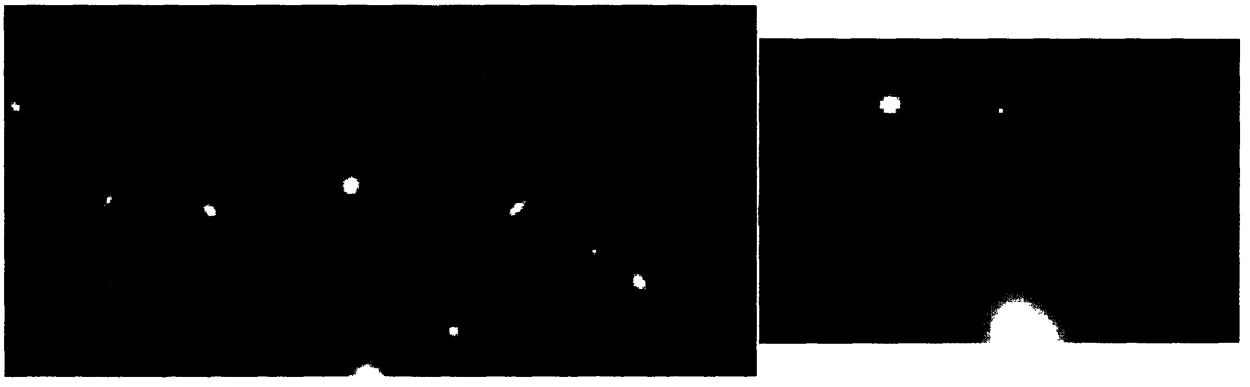

Figure 4-4: Details from Figure 1-1 of two galaxies lensed into long arcs by Abell 1689. The images measure approximately $50'' \times 20''$ and $25'' \times 15''$, on the left and right respectively.

$0.05'' \times 0.05''$ in size, while in the simulations each pixel has size $0.25'' \times 0.25''$. The larger pixel size in the simulation, necessary because of computational time limitations, effectually blurs the lensed images compared to those observed by the Hubble, grouping many pixels into one. Thus, if images from the HST and simulation appear equally smooth, it is likely that the image from the HST observation is in fact much smoother than the simulated image, which has been artificially smoothed by blurring. However, individual pixels trailing off at the ends of the lensed images, apparent in the simulated images, are likely to be unobservable in the Hubble images due to background noise and other sensitivity constraints, serving to make the observed HST images perhaps look smoother than they really are. Of these two opposing systematic limitations the effects of resolution blurring in the simulated images are likely to be larger than those of unobserved "lit" pixels in the HST images, at least in the quantitative measures of image quality. This blurring does not present significant problems for this investigation because we seek only to put a *lower limit* on the smoothness of the dark matter distribution (an upper limit on the allowed size of the density fluctuations in that distribution), which we can still do. Better resolution in the simulation would allow for a tighter limit and should be sought in

future research, but does not impeach the utility of our current results.

Figures 4-5, 4-6, 4-7, and 4-8 show representative image sequences for lensing by Plummer spheres with $a = 0.2\theta_s a_0$ for source radii of 10, 5, and 1 pixels, and by point-like Plummer spheres with $a = 0.02\theta_s a_0$ for a source radius of 10 pixels, respectively, and moving from the roughest mass distribution with $N = 10^2$ all the way to the smoothest at $N = 10^7$. The progression from choppy, very messy images to smooth, uniform arcs is apparent in all four sequences. The images created by the $r = 1$ pixel source are the most like those seen in the HST image, as they very long and thin. In every case, it is clear that the images become progressively smoother all the way through the $N = 10^7$ simulation, indicating that the upper limit of our computational capability represents the best limit we can place on the dark matter distribution.

Plotted in Figure 4-9 is the mean δM_{RMS}, averaged over six trials, as a function of N for NFW distributions of both sizes of Plummer spheres, with an empirically determined slope $\delta M_{RMS} \propto N^{-1/6}$. As expected, the mass distributions for a given number of Plummer spheres are significantly less smooth for the smaller spheres than for the larger ones, as the mass in each of the former types is more concentrated in space, leading to a clumpier overall distribution.

Now having quantified the deviations from a smooth mass profile for each of the distributions of Plummer spheres, it remains to quantify the quality of the images lensed by those distributions, and to finally set limits as to which mass distributions can create images like those observed by the HST. The back-projected sources for the $R_{source} = 10$ pixel, $a = 0.2\theta_s a_0$ sequence are shown in Figure 4-10; the back-projected sources for all other models can be found in Appendix A. The root-mean-square radius $\mathfrak{r}_{RMS}$ of the projected source, as well as its two relevant quadrupole moments Q_1 and Q_2, measures of image quality defined in Section 3.2.4, are given for each image. Figure 4-11 shows $\mathfrak{r}_{RMS}$ and Q_2 plotted as a function of N for six simulations with source radius $R = 10$ pixels and $a = 0.2\theta_s a_0$. Q_1 is not plotted, since it turns out not to be a useful measure of image quality, jumping up and down at various values of N and showing no apparent correlation to the quality of the lensed images. It is therefore abandoned, and $\mathfrak{r}_{RMS}$ and Q_2 are retained as the two useful measures

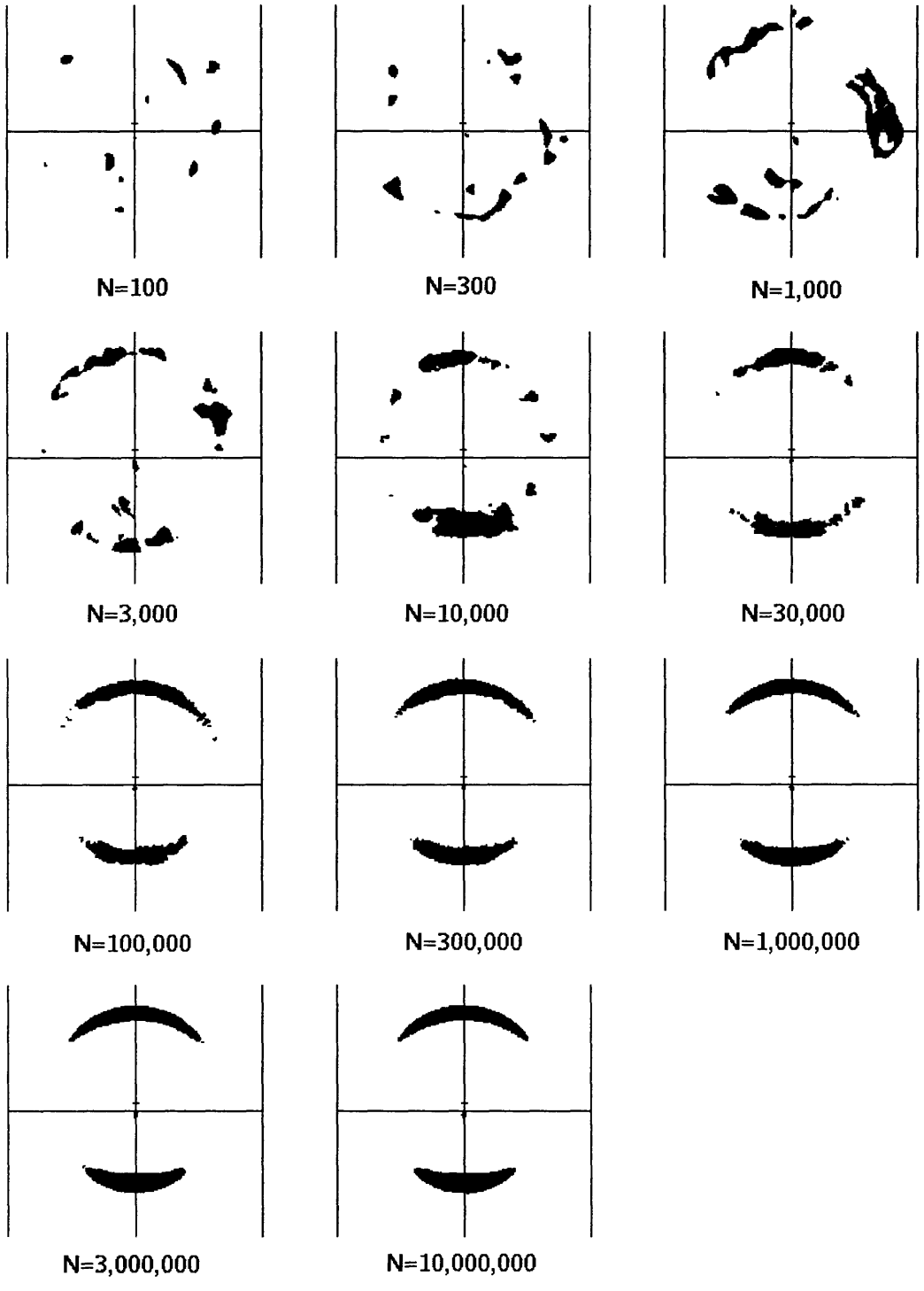

Figure 4-5: Lensed images for a source radius of 10 pixels = 2.50″, with Plummer sphere scale radius $a = 0.2\theta_s a_0$.

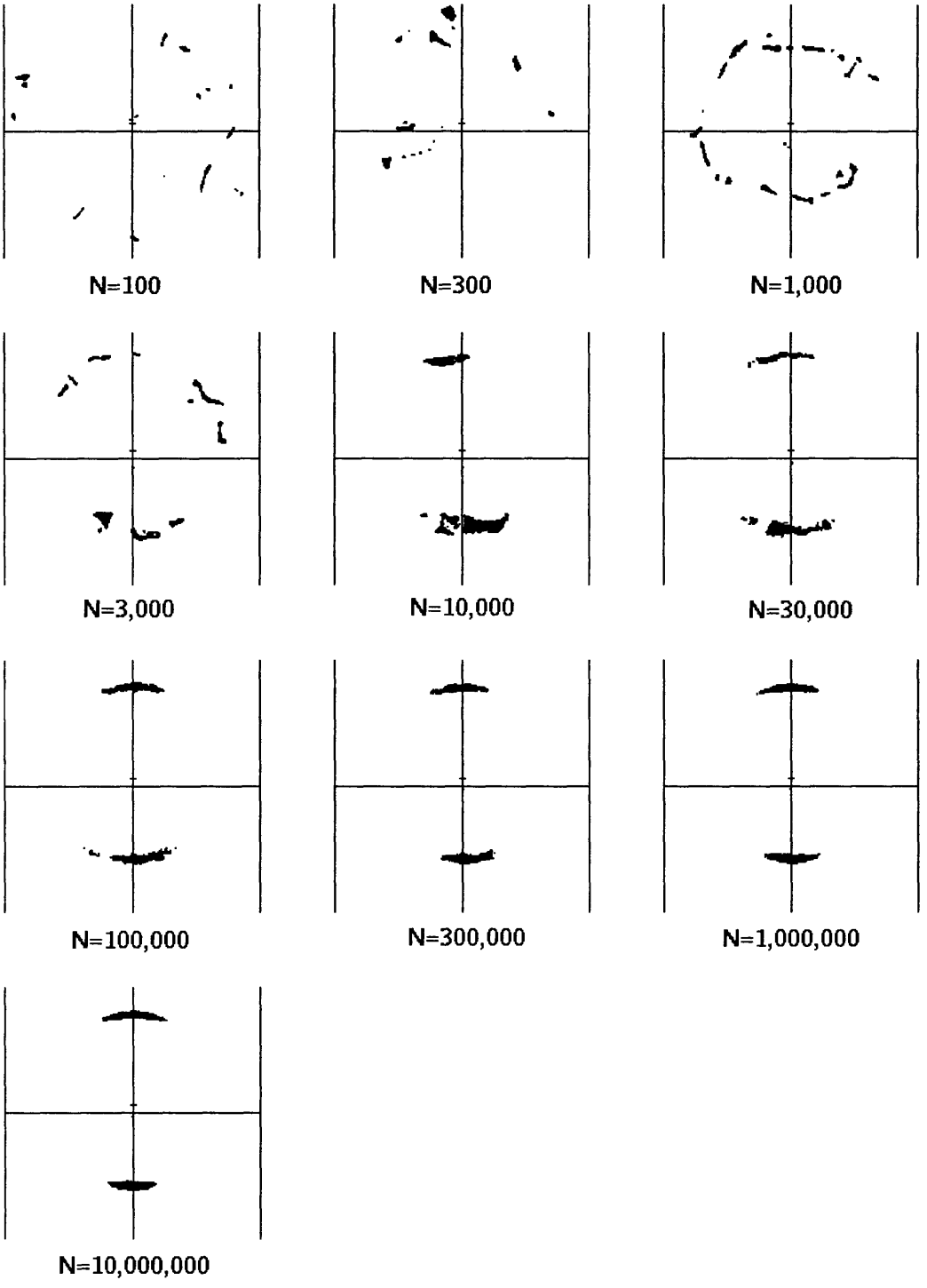

Figure 4-6: Lensed images for a source radius of 5 pixels = 1.25″, with Plummer sphere scale radius $a = 0.2\theta_s a_0$. Trials for $N = 3 \times 10^6$ did not run succesfully.

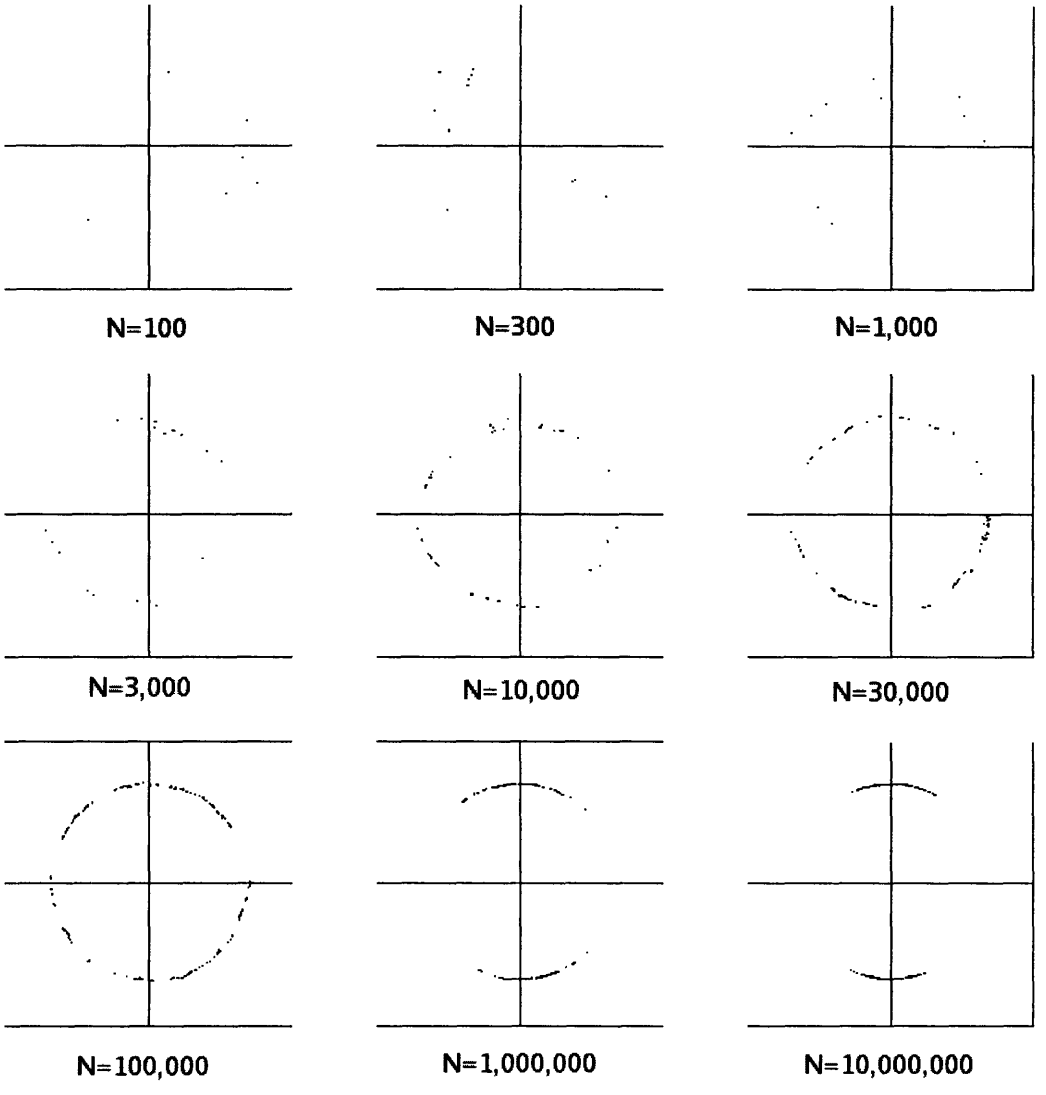

Figure 4-7: Lensed images for a source radius of 1 pixel = 0.25″, with Plummer sphere scale radius $a = 0.2\theta_s a_0$. Trials for $N = 3 \times 10^5$ and $N = 3 \times 10^6$ did not run succesfully.

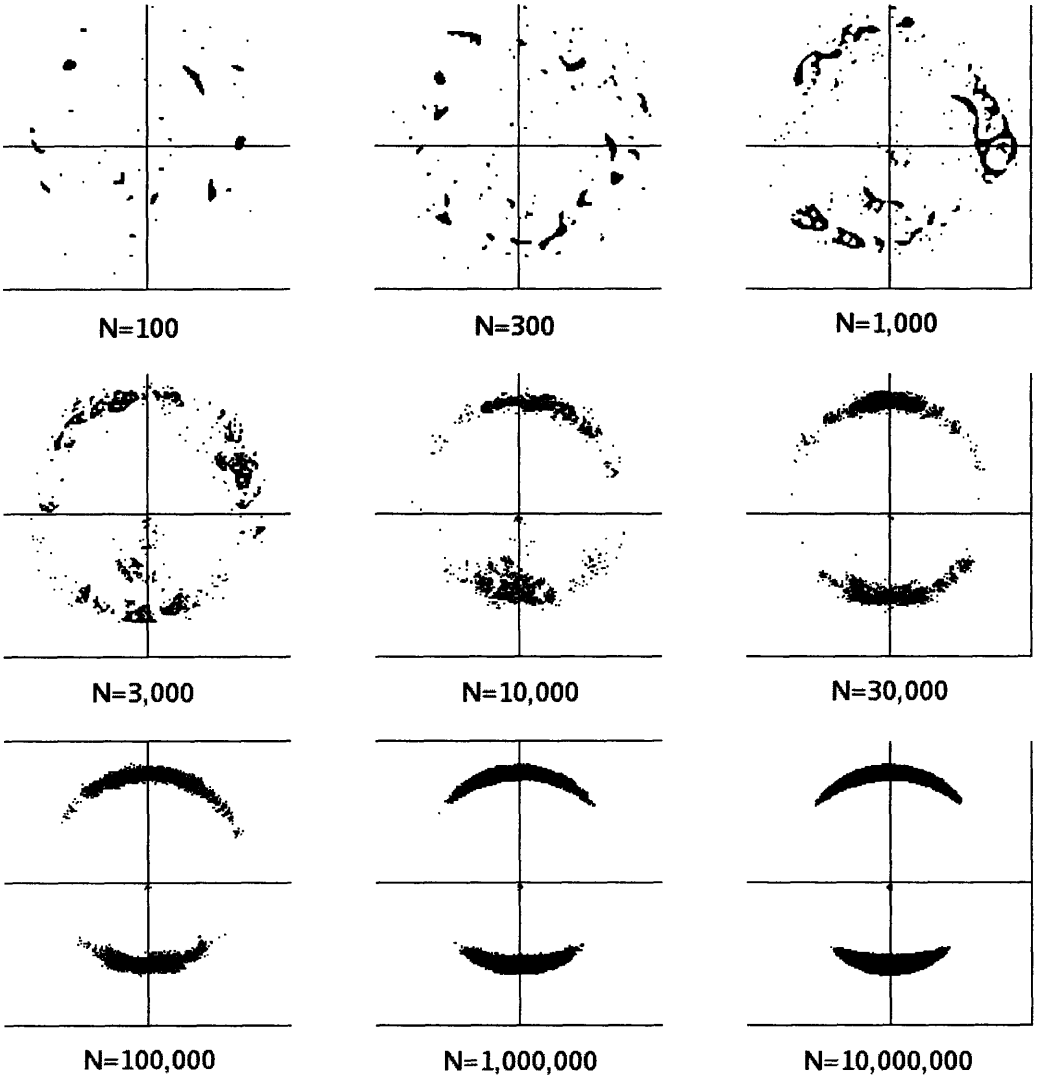

Figure 4-8: Lensed images for a source radius of 10 pixels = 2.5″, with Plummer sphere scale radius $a = 0.02\theta_s a_0$. Trials for $N = 3 \times 10^5$ and $N = 3 \times 10^6$ did not run succesfully.

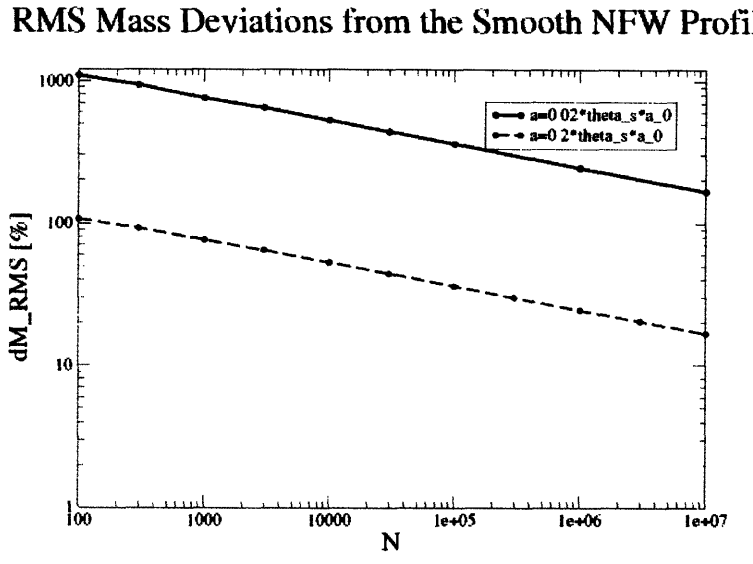

Figure 4-9: Average δM_{RMS}, measured over an annulus centered at $r = .33r_s$ of width $\sim 0.2r_s$, enclosing the lensed images, for the $a = 0.2\theta_s a_0$ Plummer sphere distributions, which fill most of space, and for the $a = 0.02\theta_s a_0$ point-like Plummer sphere distribution.

of image quality. Figure 4-12 show the behavior of these two quantities for a smaller source, which is much the same as for the source with $R = 10$ pixels.

In all four lensing scenarios both $\mathfrak{r}_{RMS}$ and Q_2 decrease as functions of both δM_{RMS} and N, as shown in Figures 4-13 and 4-14. However, the scale of δM_{RMS} is significantly larger for the scenario employing point-like Plummer spheres, with a maximum value of over 1000%, compared to a maximum for the larger Plummer spheres of just over 100%. The quality of the images does not, however, change appreciably with changing size of the Plummer spheres. Figure 4-14 shows that indeed, as a function of N, all four models behave very much the same, both qualitatively and quantitatively. This suggests that density deviations from the smooth mass distribution on small spatial scales (i.e., the scale of individual pixels) are not significant in determining the quality of images, but only the relatively large scales corresponding to the distances between the centers of the Plummer spheres. This behavior strongly suggests that it is the number of Plummer spheres, and thus their individual masses,

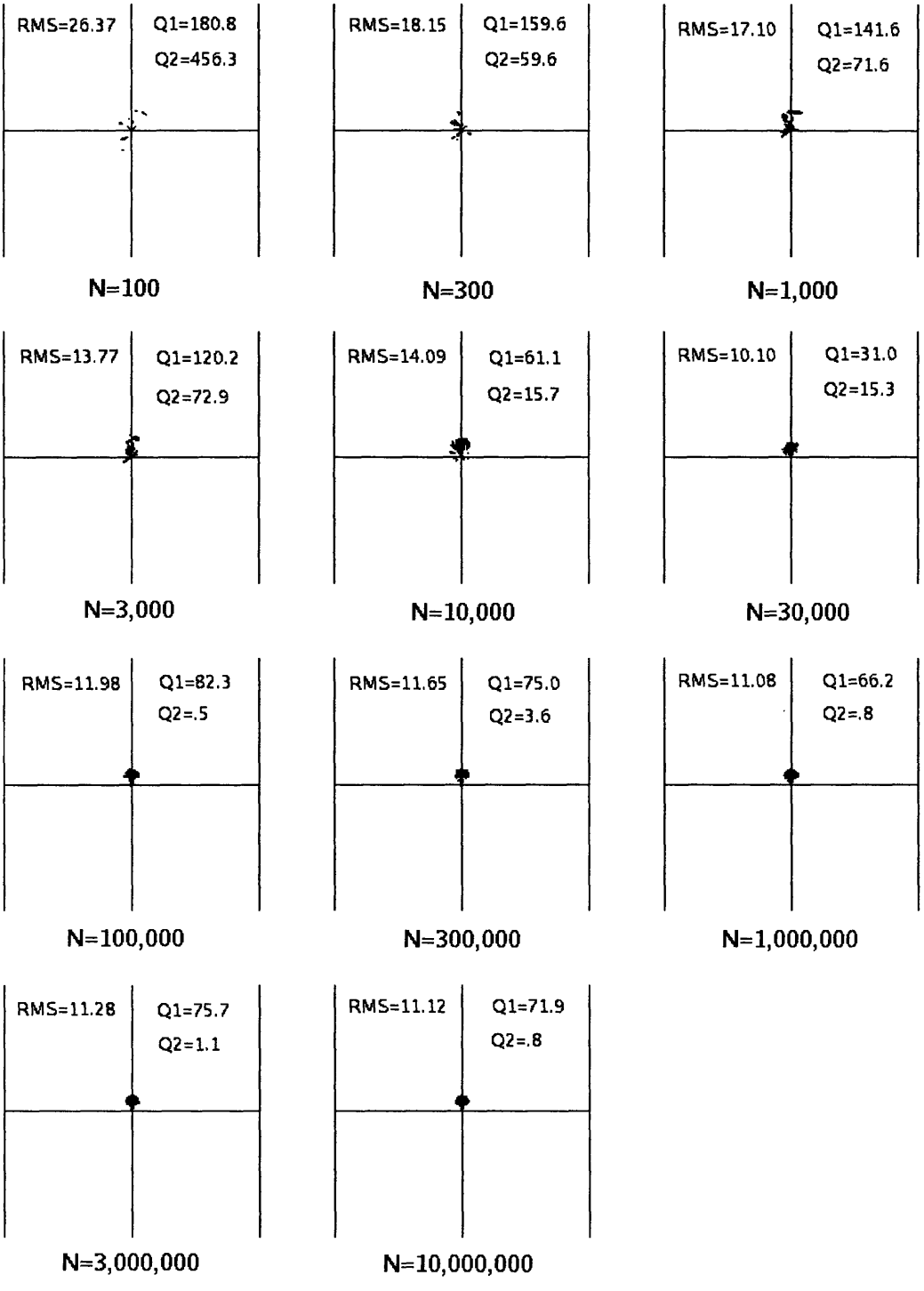

Figure 4-10: The back-projected sources of lensed images of a source of radius of 10 pixels = 2.50″, projected back into the source plane through a smooth NFW lensing profile.

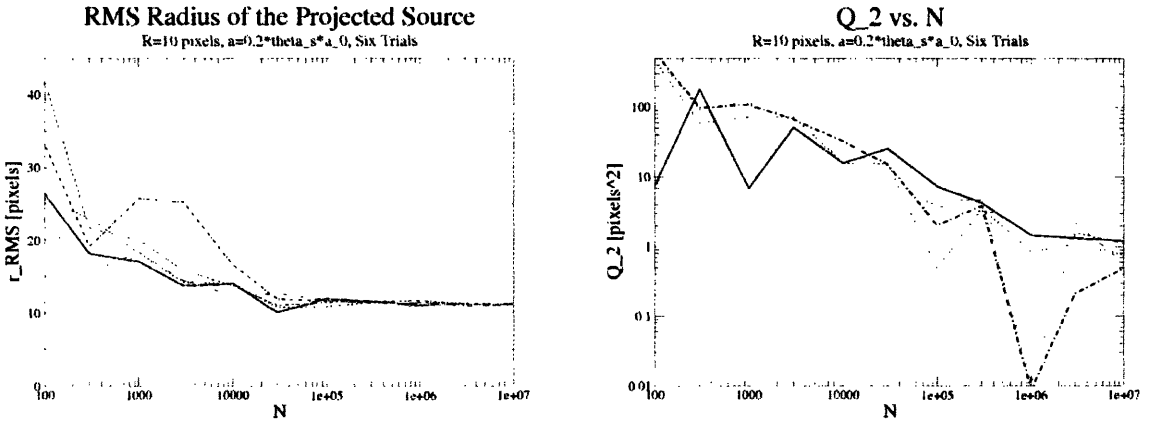

Figure 4-11: Plots of $\mathfrak{r}_{RMS}$ and Q_2 as a function of N for a source with $R = 10$ pixels and $a = 0.2\theta_s a_0$ for six different random mass distributions.

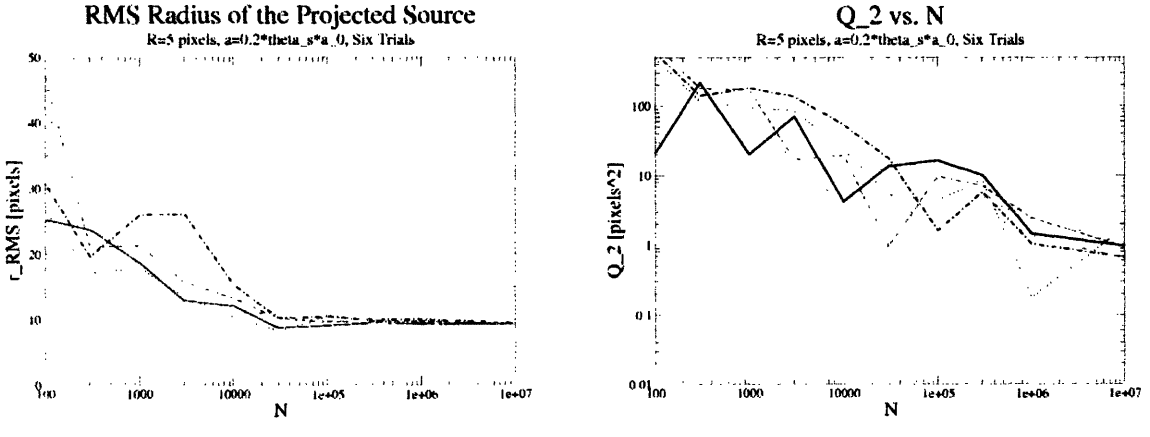

Figure 4-12: Plots of $\mathfrak{r}_{RMS}$ and Q_2 as a function of N for a source with $R = 5$ pixels and $a = 0.2\theta_s a_0$ for six different random mass distributions.

but not their spatial extent that is the critical variable in shaping strong lensing outcomes.

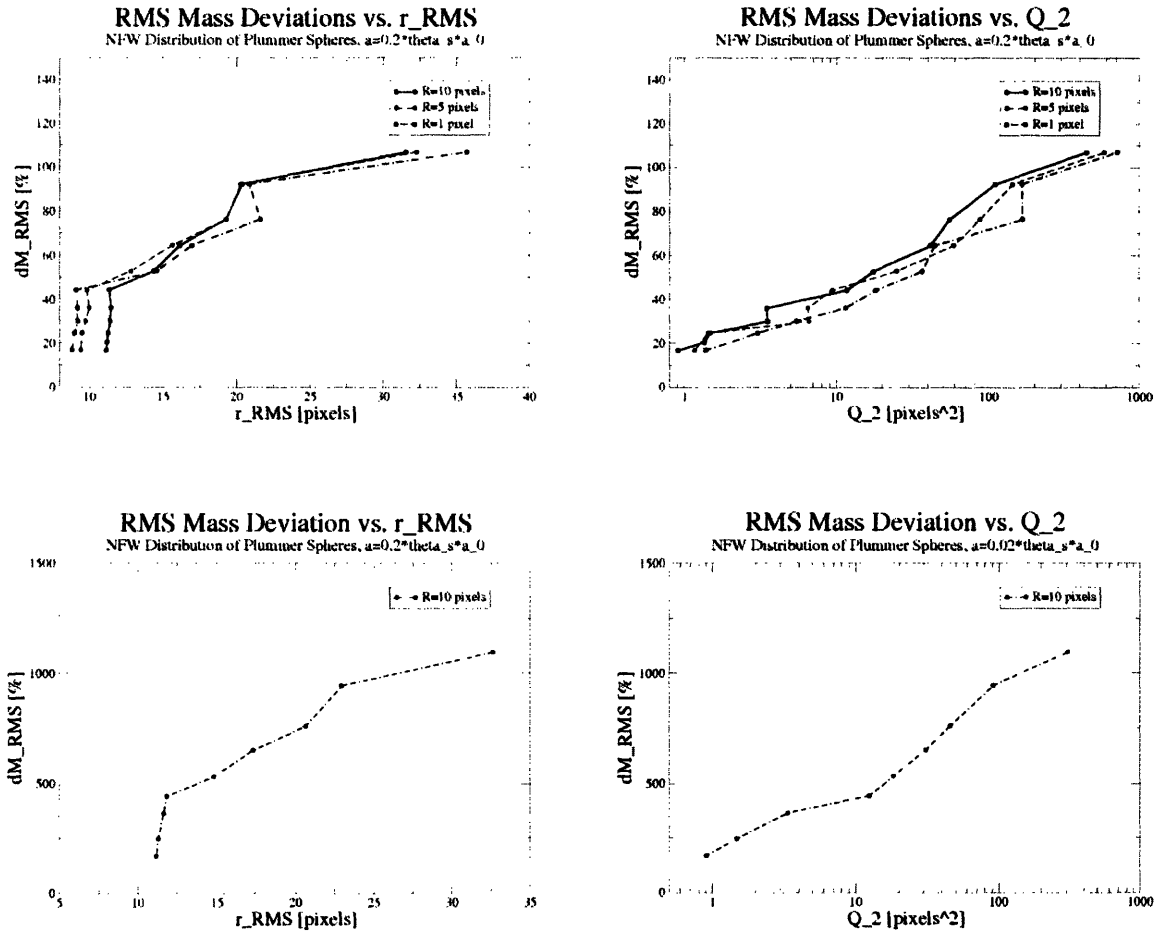

Figure 4-13: δM_{RMS} as a function of the mean $\mathfrak{r}_{RMS}$ and Q_2 for all four lensing models. Note the very different scales of the mass deviations for the larger Plummer spheres as compared to those for the point-like masses, as well as the similarity of the qualitative behavior.

The lensing behavior of the large and small Plummer sphere distributions can be understood by considering the regimes of micro- and strong lensing. If one examines the full arrays of images for all four scenarios, it is apparent that at low to mid-range N the images created by the distributions of point-like Plummer spheres look different from those created by the distributions of larger spheres, with many more

individually "lit" pixels speckling the image. This is the result of micro-lensing by the individual point-like Plummer spheres, for which $a < \theta_E$ and such lensing is possible. As expected, the number of the speckles decreases with increasing N as the Einstein radii of the individual spheres become ever smaller than the source radius. By contrast, in the distribution of larger spheres no such speckles are seen; only strong lensing occurs because the individual Plummer spheres are too large to micro-lens on their own. When very large number of spheres are used, the effects of micro-lensing are washed out by the strong lensing properties of the whole cluster, and thus the behavior of the two types of distributions converges at large N.

Looking more closely at $\mathfrak{r}_{RMS}$ and Q_2 as functions of N, it is apparent that $\mathfrak{r}_{RMS}$ flattens out considerably at high -N, and is no longer able to consistently differentiate between images created by profiles of large numbers of Plummer spheres ($N = 10^6$, $N = 10^7$). However, Q_2, when plotted log-log with N, shows a consistent power law relationship with the number of Plummer spheres for all values of N, all the way through $N = 10^7$, suggesting that it remains a useful measure of quality. Visual examination of the images also suggests a continued smoothing all the way through $N = 10^7$, and Q_2 confirms that indeed image quality is still improving. We are therefore inclined to set the minimum number of mass elements for high-quality images at $N = 10^7$. However, because the differences visible between the $N = 10^6$ and $N = 10^7$ lensed images consist largely of isolated pixels at the ends of the lensed arcs, and as discussed above, such pixel-sized image imperfections would likely be invisible in the HST observations, it seems prudent to relax the limit. We therefore conclude that there must be at least 10^6 Plummer sphere-equivalents within a projected angular radius of $0.67\theta_s$ from the galaxy cluster's center in order to obtain smooth images comparable to those observed in nature.

4.4 Conclusions

In a distribution of 10^6 Plummer spheres each Plummer sphere has a mass of 3.5×10^8 $M_\odot$. Though actual dark matter is not likely to be distributed in finite Plummer

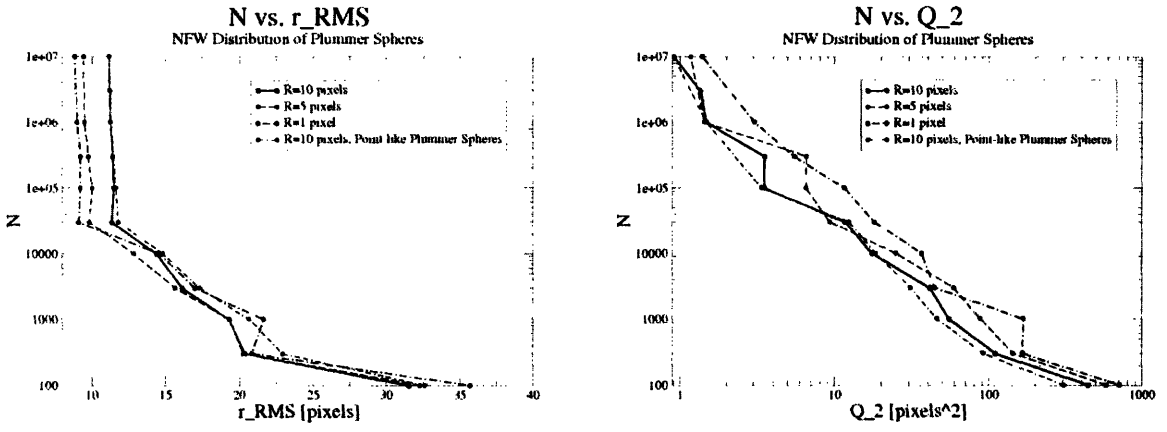

Figure 4-14: N as a function of the mean $\mathfrak{r}_{RMS}$ and Q_2 for all four lensing models. Note the similarity of the quantitative behavior across all four models.

spheres throughout the galaxy cluster, the fact that our results are approximately independent of the spatial distribution of the mass within each mass element does imply a universal constraint on the scale of the physically allowed mass fluctuations in the NFW dark matter profiles of galaxy clusters: each mass element must be $\lesssim 4\times10^8\ M_\odot$. Mass fluctuations in the surface density on spatial scales of ~ 0.22 kpc$\times$ 0.22 kpc are not important to strong lensing; rather it is larger fluctuations on the scales of the spacings between the 10^6 mass elements–in the surface density areas of order 500 pc $\times$ 500 pc and in the three dimensional NFW distribution volumes of 10 kpc $\times$ 10 kpc $\times$ 10 kpc–that determine the lensing behavior of the cluster. Thus we conclude that the dark matter in galaxy clusters must be distributed quite smoothly over scales of order 10 kpc$\times$10 kpc$\times$10 kpc, but may be lumpy on smaller scales, with mass "clumps" in the smooth NFW surface density profile no larger than $\sim 10^8\ M_\odot$.

The key requirement for further tightening this upper limit on dark matter "clumps" within a smooth dark matter NFW distribution in galaxy clusters is the introduction of a larger calculation grid with smaller pixels, closer in size to those in the HST images. This requires a more efficient computing strategy and more computing time. As well, further testing of the allowed spatial scale of mass fluctuations would be useful to confirm the findings of this thesis that strong gravitational lensing is not sensitive

to spatial fluctuations on scales smaller than 500 pc $\times$ 500 pc, using a wide range of spatial sizes for the mass elements. Furthermore, a different measure of image quality, more sensitive to small imperfections than τ_{RMS}, is a necessary complement to Q_2 in quantizing the quality of images created by large-N distributions, important to any improvement of the dark matter distribution smoothness limit using the methods of this research. Such a measure might require quantifying the uniformity of the image in the image plane itself, rather than simply projecting back to the source plane; one such candidate is a quantity that measures the ratio of the edges of the image to its total area. Once equipped with these better measures of quality, simulations of larger numbers of individual mass elements might prove useful to tighten the limit on the smoothness of the dark matter distribution in galaxy clusters, set by this research to be mass "clumps" no larger than 10^8 $M_\odot$ over scales of 10 kpc $\times$ 10 kpc $\times$ 10 kpc.

Appendix A

Back-Projected Sources

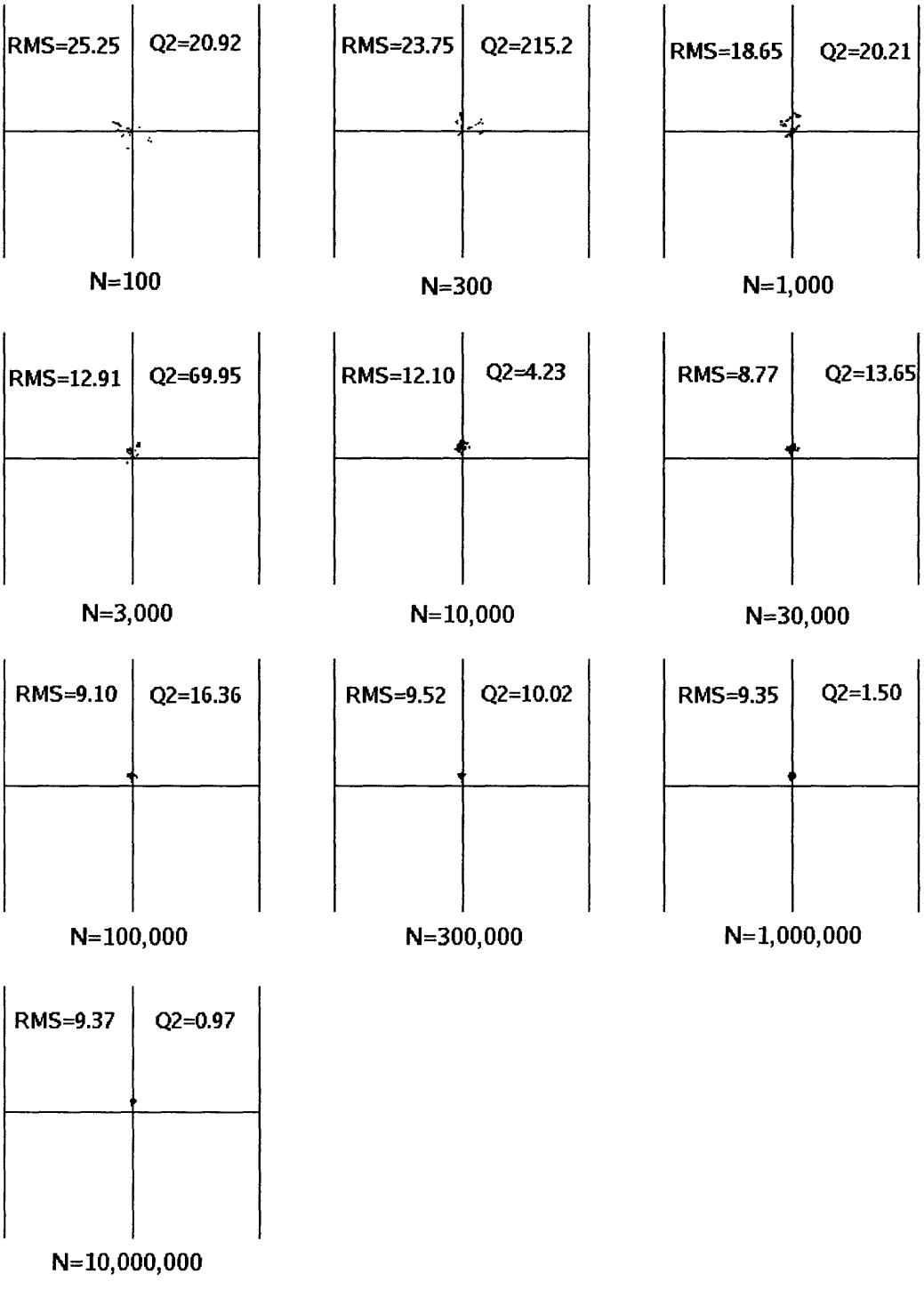

Figure A-1: The projected sources of lensed images of a source of radius of 5 pixels $= 1.25''$, $a = 0.2\theta_s a_0$, projected back into the source plane through a smooth NFW lensing profile.

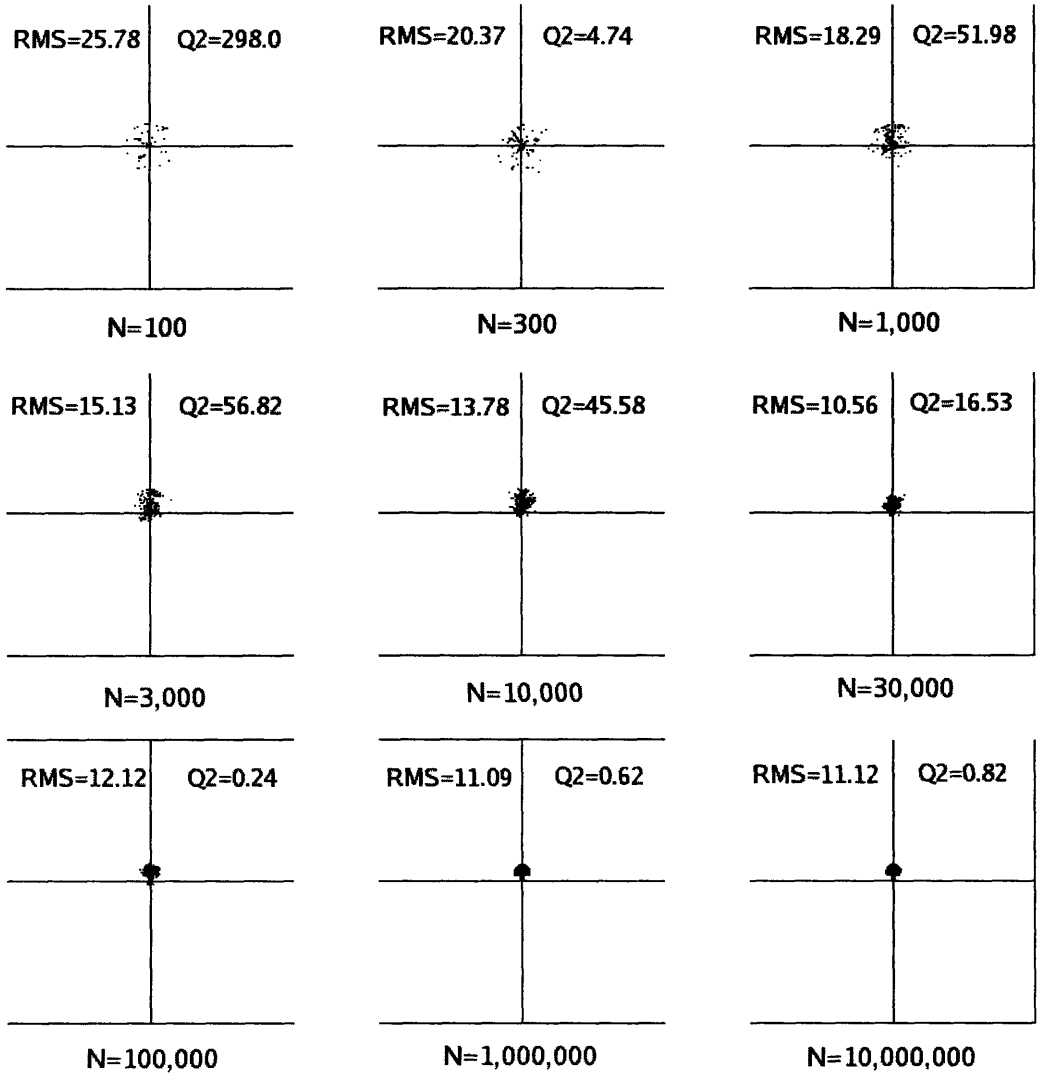

Figure A-2: The projected sources of lensed images of a source of radius of 10 pixels $= 2.50''$, $a = 0.02\theta_s a_0$, projected back into the source plane through a smooth NFW lensing profile.

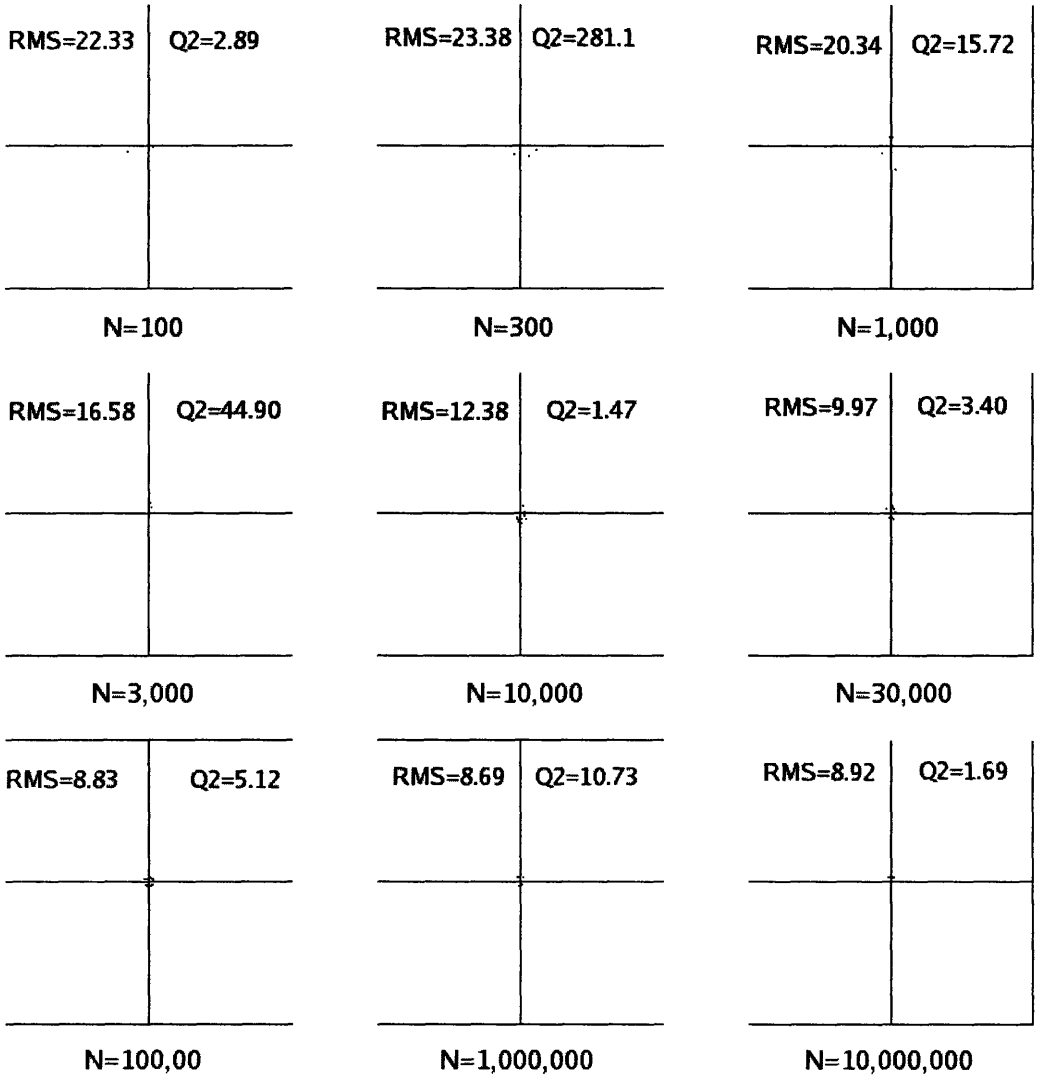

Figure A-3: The projected sources of lensed images of a source of radius of 1 pixel $0.25''$, $a = 0.2\theta_s a_0$, projected back into the source plane through a smooth NFW lensing profile.

Bibliography

[1] James Binney and Scott Tremaine. *Galactic Dynamics*, chapter 2.2. Princeton University Press, 1988.

[2] T. Broadhurst et al. Strong Lensing Analysis of A1689 from Deep Advanced Camera Images. *The Astrophysical Journal*, 621(1):53–88, 2005.

[3] Randall L. Cooper. History, Overview, and Basic Theory of Gravitational Lensing. *Class Notes from Astronomy 200. Seminar in Modern Astrophysics at Harvard University*, February 2004.

[4] Scott Dodelson. *Modern Cosomology*, chapter 2.4. Academic Press, 2003.

[5] A. H. Guth. Inflationary universe: A possible solutions to the horizon and flatness problems. *Physical Review D (Particles and Fields)*, 23(2):347–356, January 1981.

[6] J.N. Hewitt, E.L. Turner, D.P. Schneider, B.F. Burke, G.I. Langston, and C.R. Lawrence. Unusual Radio Source MG 1131+0456: a possible Einstein Ring. *Nature*, 333:537, 1988.

[7] D. W. Hogg. Distance Measures in Cosmology. *(astro-ph/9905116)*, December 2000.

[8] C. R. Keeton. A Catalog of Mass Models for Gravitational Lensing. *Preprint (astro-ph/0102341)*, June 2002.

[9] R. Lynds and V. Petrosian. Giant Luminous Arcs in Galaxy Clusters. *Bulletin of the American Astronomical Society*, 18:1014, 1986.

[10] J. F. Navarro, C. S. Frenk, and S. D. M. White. The structure of cold dark matter halos. *The Astrophysical Journal*, 462:563, 1996.

[11] John A. Peacock. *Cosmological Physics*, chapter 9.5. Cambridge University Press, 1998.

[12] William H. Press, Saul A. Teukolsky, William T. Vetterling, and Brian P. Flannery. *Numerical Recipes in C*, chapter 7.0-7.3. Cambridge University Press, 2002.

[13] V.C. Rubin. The rotation of spiral galaxies. *Science*, 220:1339–1344, June 1983.

[14] Paul L. Schechter. *Class Notes from 8.284 Modern Astrophysics at MIT*. April 2005.

[15] D. Sluse et al. A quadruply imaged quasar with an optical Einstein ring candidate, 1RXS J113155.4-123155. *Astronomy and Astrophysics*, 406:L43–L46, 2003.

[16] D.N. Spergel et al. First-Year Wilkinson Microwave Anisotropy Probe (WMAP) Observations: Determination of Cosmological Parameters. *The Astrophysical Journal Supplement Series*, 148(1):175–194, 2003.

[17] D. Walsh, R.F. Carswell, and R.J. Weymann. 0957+561 {A},{B}: twin quasistellar objects or gravitational lens? *Nature*, 279:381–384, May 1986.

[18] R.J. Weymann et al. The triple QSO PG 1115+08 - Another probable gravitational lens. *Nature*, 285:641–643, 1980.

[19] F. Zwicky. On the Masses of Nebulae and of Clusters of Nebulae. *The Astrophysical Journal*, 86:217, 1937.